Micromechanics of brittle faulting and cataclastic flow in Alban Hills tuff

Wei Zhu,[1] Patrick Baud,[2] Sergio Vinciguerra,[3] and Teng-fong Wong[1]

Received 13 October 2010; revised 14 March 2011; accepted 29 March 2011; published 25 June 2011.

[1] An understanding of how tuff deforms and fails is of importance in the mechanics of volcanic eruption as well as geotechnical and seismic applications related to the integrity of tuff structures and repositories. Previous rock mechanics studies have focused on the brittle strength. We conducted mechanical tests on nominally dry and water-saturated tuff samples retrieved from the Colli Albani drilling project, in conjunction with systematic microstructural observations on the deformed samples so as to elucidate the micromechanics of brittle failure and inelastic compaction. The phenomenological behavior was observed to be qualitatively similar to that in a porous sedimentary rock. Synthesizing published data, we observe a systematic trend for both uniaxial compressive strength and pore collapse pressure of nonwelded tuff to decrease with increasing porosity. To interpret the compaction behavior in tuff, we extended the cataclastic pore collapse model originally formulated for a porous carbonate rock to a dual porosity medium made up of macropores and micropores or microcracks.

Citation: Zhu, W., P. Baud, S. Vinciguerra, and T. Wong (2011), Micromechanics of brittle faulting and cataclastic flow in Alban Hills tuff, *J. Geophys. Res.*, *116*, B06209, doi:10.1029/2010JB008046.

1. Introduction

[2] Tuffs are consolidated pyroclastic or volcaniclastic rocks [*Fisher et al.*, 2006]. Since they are the products of explosive volcanic eruptions, tuff deposits may disperse widely and blanket vast areas (~10^2–10^3 km^2) in a considerable thickness (~100 m). There are 41 large industrial cities in 24 nations (including two megacities) that are underlain or partly underlain by tuffs [*Heiken*, 2006]. Since the ejected pyroclasts and volcaniclastic could subsequently be welded and cemented to different degrees, they form consolidated rocks that span a broad spectrum of porosity and mechanical strength. In some cases, tuffs can result from repeated pyroclastic flows in which the surface cools more rapidly and becomes less vitrified than the base, leading to small-scale variations in physical properties within the tuff unit. Many of the well-consolidated tuffs are sufficiently strong for use in the construction of buildings and structures for thousands of years [*Funiciello et al.*, 2006].

[3] A proposed repository for high-level nuclear waste in the USA is located in a tuff formation in Yucca Mountain, Nevada [*Long and Ewing*, 2004]. A challenging seismological question for this repository is estimation of the physical limit on extremely large ground motion associated with earthquake hazards [*Andrews et al.*, 2007; *Templeton et al.*, 2010]. *Andrews* [2007] recently suggested that since this estimate is sensitively dependent on how the porous tuff yields in compaction, pertinent mechanical data are required to constrain realistically the modeling of ground motion [*Lockner and Morrow*, 2008]. Hence it is important to have a fundamental understanding of the mechanical and hydraulic properties of tuffs, which can provide useful insights and constraints on the physics of volcanic eruption, as well as geotechnical and seismic applications related to the integrity of tuff structures and repositories.

[4] Previous rock mechanics studies of tuff have focused on the brittle strength, and most are site specific. A common observation is that tuff strength can be highly variable at a given site. In her comprehensive study of ignimbrite (a pyroclastic deposit or "ash flow tuff") in New Zealand, *Moon* [1993a, 1993b] observed very rapid vertical variations in uniaxial compressive strength, by as much as two orders of magnitude in core samples retrieved within one vertical section. While there may be an overall trend for the strength to decrease with increasing porosity, other microstructural attributes (including the nature of welding, microcrack density, as well as the presence of lithophysae, pumice and clay minerals) seem to also exert important influence [*Price and Bauer*, 1985; *Moon*, 1993a; *Schultz and Li*, 1995; *Evans and Bradbury*, 2004; *Avar and Hudyma*, 2007]. In particular, welded tuffs (the fragments of which were plastic enough when they were deposited to have been fused) may show significant variability in strength even if they have comparable porosities.

[5] Possibly because of its material complexity and mechanical variability, there is a paucity of microstructural observations on the damage development associated with

[1]Department of Geosciences, State University of New York at Stony Brook, Stony Brook, New York, USA.
[2]Institut de Physique du Globe de Strasbourg, UMR 7516 CNRS, EOST, Université de Strasbourg, Strasbourg, France.
[3]Istituto Nazionale di Geofisica e Vulcanologia, Sezione di Roma1, Rome, Italy.

0148-0227/11/2010JB008046

brittle failure in tuff. In the absence of such observations, it is very difficult to place any constraints on the micromechanics of brittle failure in tuff and to assess whether some of the existing damage mechanics models (primarily developed for application to compact crystalline rocks or porous sedimentary rocks) are applicable to tuff. A first objective of this study is therefore to conduct mechanical tests on tuff samples retrieved from the Colli Albani (Rome, Italy) drilling project [*Mariucci et al.*, 2008], in conjunction with systematic microstructural observations on the deformed samples so as to elucidate the micromechanics of brittle failure. We deformed samples from two blocks of tuff, with average porosity of 32% and 37%, respectively. Both nominally dry and water-saturated samples were studied.

[6] Partly because of its relative high porosity, tuff undergoes a transition in failure mode from brittle fracture to cataclastic flow with increasing confinement at room temperature. In this study we conducted conventional triaxial compression experiments over a sufficiently broad range of pressure so that this phenomenon of low-temperature brittle-ductile transition can be observed. The macroscopic mechanical behavior (involving shear-enhanced compaction and strain hardening) was observed to be qualitatively similar to that in a porous sedimentary rock such as sandstone [*Wong et al.*, 1997] or limestone [*Vajdova et al.*, 2004], with the implication that some of the phenomenological models developed for these rocks [e.g., *Ricard and Bercovici*, 2003; *Hamiel et al.*, 2004; *Sleep*, 2010] can also be used for the constitutive modeling of tuff deformation.

[7] Notwithstanding the similarities in their phenomenological behaviors, the micromechanics of compaction in clastic and carbonate rocks have recently been demonstrated to be quite different. In a clastic rock such as sandstone, inelastic compaction in a laboratory sample derives primarily from grain crushing initiated by the stress concentrations at grain contacts that induce intragranular cracks to radiate in a conical pattern toward the interior of the impinging grains [*Menéndez et al.*, 1996]. In contrast, microstructural observations have shown that inelastic compaction in limestone is associated with pore collapse, that seems to initiate from stress concentrations at the surface of an equant pore, which induce a ring of localized damage in its periphery [*Zhu et al.*, 2010]. Whether these two fundamentally different micromechanical processes are at all relevant to tuff compaction is a question that can be addressed only if systematic microstructural observations have been conducted on the deformed samples. Accordingly a second objective of this study is to investigate the phenomenology and micromechanics of inelastic compaction and cataclastic flow in the Alban Hills tuff. Synthesizing our data with other published mechanical data, we assess to what extent the micromechanical processes associated with brittle fracture and compactive cataclastic flow in tuff can be analyzed with some of the existing damage mechanics models.

2. Experimental Procedure

2.1. Alban Hills Volcanic Complex

[8] The geologic foundation of Rome is mostly composed of tuffs from the Colli Albani (Alban Hills) volcanic field in the southeastern part of the present city, and to a less extent, from the Sabatini field in the northwest. Alban Hills is part of a chain of mainly explosive volcanic districts and small eruptive centers that developed along the Tyrrhenian margin of central Italy over a distance of ~200 km since the Middle Pleistocene. Extensional faults associated with the Apennic orogeny and subsequent opening of the Tyrrhenian Sea follow a regional trend along the NW-SE direction, which is intersected by a local N-S, right-lateral fault system developed behind the Olevano-Antrodoco thrust front [*de Rita and Giampaolo*, 2006; *Vinciguerra et al.*, 2009]. Recent seismic swarms and hydrothermal activity at the Alban Hills volcanic complex have triggered the interest to gain a deeper understanding of the volcanic and seismic hazards it may pose to Rome and its vicinity. A scientific drilling project involving a 350 m borehole was accordingly undertaken to elucidate the inner structure of this volcanic field [*Mariucci et al.*, 2008].

[9] The volcanic history of Alban Hills may be roughly divided into three main phases that were separated by two periods of dormancy with durations on the order of 10^3 years. The early Tuscolano-Artemisio Phase (~561–366 ka) with five large pyroclastic eruptions was the most explosive and voluminous (with cumulative volume on the order of 10 km^3). The second Faete Phase (~308–250 ka) was less energetic, and the Late Hydromagmatic Phase (~200–36 ka) was dominated by pyroclastic surges. The main lithology penetrated by the Colli Albani drilling project was the tuff deposited during the Tuscolano-Artemision Phase, which exhibited a wide variability in grain size and cohesion [*Mariucci et al.*, 2008]. Since the nonwelded tuff was primarily deposited by pyroclastic flow, it can also be categorized as an ignimbrite [*Funiciello et al.*, 2006].

2.2. Sample Material and Preparation

[10] Figure 1 [after *Vinciguerra et al.*, 2009] illustrates schematically the stratigraphy of volcanic units encountered by the Colli Albani borehole. One of our ignimbrite blocks was retrieved from ~137 m in the Tufo Pisolitico di Trigoria unit. During the Archaic period Tufo Pisolitico was a primary building stone for the infrastructure of Rome [*de Rita and Giampaolo*, 2006]. Our block is from an interval 12.4 m thick that was described by *Mariucci et al.* [2008, p. 164] as "light gray, indurate, matrix-supported, coarse-ash deposit with leucite, mm-to-cm-sized gray scoria clasts and sedimentary lithics, accretionary lapilli, enriched in carbonate lithics in the base."

[11] Our second block was retrieved from a depth of ~107 m in the Tufo del Palatino unit, within an interval 22.2 m thick that was described by *Mariucci et al.* [2008, p. 164] as "dark gray, massive, indurate, matrix-supported, coarse-ash, with leucite and clinopyroxene, abundant mm-to-cm-sized gray and yellow scoria clasts, lava and sedimentary lithics." A full petrographic description has been presented for these lithologies by *Palladino et al.* [2001]: Submillimetric euhedral crystals of leucite (Lc), scarce clinopyroxene (Cpx) and apatite (Ap) impart sparsely porphyritic textures (<10% by volume of phenocrysts) to juvenile scoria lapilli. Rare scoria lapilli contain phlogopite (Phl) and also Timagnetite (Ti-Mt). The peculiar chemical composition of juvenile scoria clasts from pyroclastic deposits of the Alban Hills (i.e., high Al/Si ratio similar to that of zeolite network) has favored the more or less

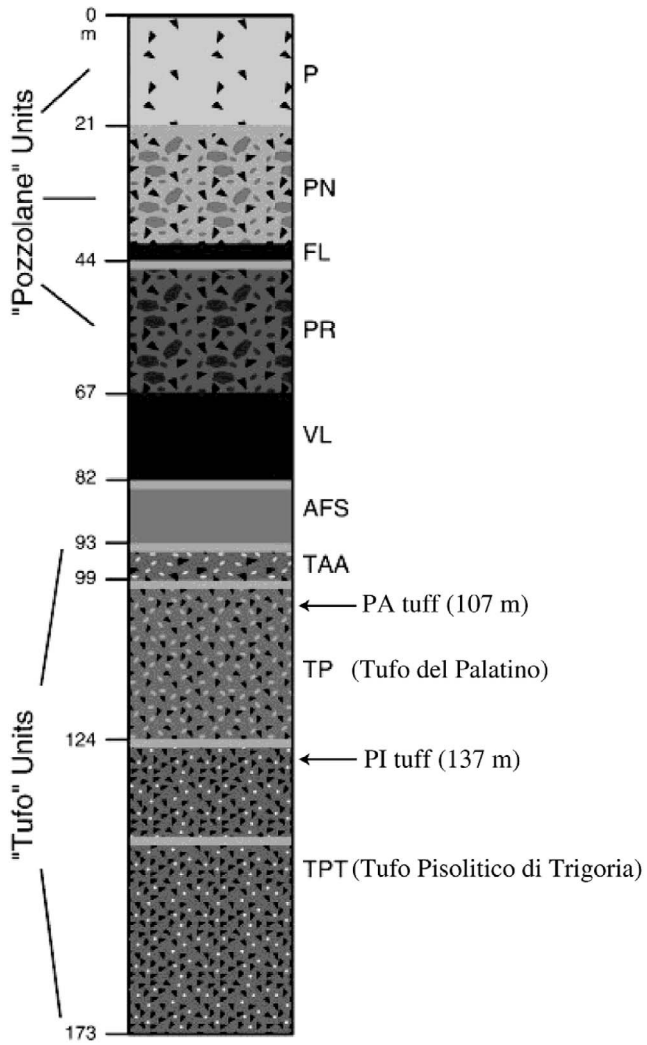

Figure 1. Schematic stratigraphy of volcanic units encountered by the Colli Albani borehole [after *Vinciguerra et al.*, 2009]. TP and TPT represent "Tufo del Palatino" and "Tufo Pisolitico di Trigoria" unit, respectively. Our samples drilled from these two units are correspondingly denoted by PA and PI tuff. The drilling depths are indicated by arrows.

complete postdepositional transformation of glass into phillipsite and/or chabazite. While the compositions of the two blocks are quite similar, there is an overall trend for the Tufo Pisolitico block to be more porous than the Tufo del Palatino block. In this paper, samples from these two blocks will be denoted by PI and PA, respectively.

[12] Hydrostatic and triaxial compression experiments were performed on nominally dry and water-saturated samples. The PA samples were all deformed in the Stony Brook laboratory, as were two PI samples that were hydrostatically compacted. Nonhydrostatic deformation experiments on the PI tuff were performed in the Institut de Physique du Globe de Strasbourg. A total of 11 PA and 7 PI tuff samples were deformed, and petrographic thin sections of 9 of these deformed samples were prepared for microstructural observations. Before deformation, the density of the vacuum dried sample was determined. The connected porosities of selected samples were also measured by water saturation (Table 1). For comparison, the porosity of one sample from each block was also measured by a pycnometer. Values of 32% and 37% were so determined for the PA and PI samples, respectively. The pycnometer measurements also gave the average density of the solid grains, which we can use to infer the porosity from the dry density of a sample. In coring from the tuff blocks, we attempted to obtain relatively homogenous samples not including some of the larger scoria clasts. Nevertheless, two of our samples (Td1_PI and Td2_PI) were quite heterogeneous, with one or more such clasts visible on the sample surfaces. The inferred porosities of these two are much lower than the other Tufo Pisolitico samples.

[13] The Stony Brook and Strasbourg laboratories followed similar sample preparation and experimental protocol. However, dimensions of the cylindrical specimens were different: in Stony Brook the specimens had initial diameter of 18.4 mm and length of 38.2 mm, whereas those in Strabourg had diameter of 20 mm and length 40 mm. For a wet experiment the sample was first dried in vacuum at 80°C for 48 h, then saturated with deionized water. Each sample was jacketed with a thin copper foil of thickness 0.05 mm and placed between two steel end plugs, one of which has a piezoelectric transducer (PZT-7, 5.0 mm diameter, 1 MHz longitudinal resonant frequency) on its flat surface, and the other one has a concentric hole for fluid access to the pore pressure system. Heat shrink polyolefine tubing was used to separate the sample from confining pressure medium (kerosene). For a nominally dry test the sample was dried in vacuum at 80°C for several days. Electric resistance strain gages (TML type PFL-10-11) were attached to the copper jacket to measure the axial and transverse strains. The strain gages were easily broken due to pore collapse near the sample surface. To circumvent the problem, we followed the procedure of *Vajdova et al.* [2004]: after the sample had been pressurized to 5 MPa, the larger surface pores were filled with a high-viscosity epoxy. The sample was then jacketed with copper foil, and a small hydrostatic pressure was applied to "season" the copper jacket before two strain gages were glued to its surface in orthogonal directions.

2.3. Mechanical Deformation

[14] The jacketed samples were deformed in the conventional triaxial configuration at room temperature. The triaxial experiments were conducted at confining pressures ranging from 5 MPa to 45 MPa for nominally dry samples and at effective pressures ranging from 5 MPa to 30 MPa for saturated samples. One dry sample of each block was also deformed without any confinement. The confining pressure was monitored by a strain gage pressure transducer to accuracy of 0.1 MPa, and during triaxial loading it was held constant to within 1%. The axial load was measured with an external load cell with an accuracy of 1 kN. The axial displacement was servo controlled at a fixed rate (corresponding to a nominal strain rate of 1.2×10^{-5} s^{-1}).

[15] Experiments on the saturated samples were conducted at a fixed pore pressure of 10 MPa, and the strain rate was sufficiently slow for the deformation to be under fully drained conditions. Adjustment of a pressure generator kept the pore pressure constant, and the pore volume change was recorded by monitoring the piston displacement of the pressure generator with a displacement transducer (DCDT).

Table 1. Stress History of Samples Studied

Sample	Density (g/cm^3)	Porosity (%)	Effective Pressure (MPa)	Peak Stress (MPa)		Critical Yield Stress (MPa)	
				Differential Stress σ_1-σ_3	Effective Mean Stress $(\sigma_1 + 2\sigma_3)/3$-P_p	Differential Stress σ_1-σ_3	Effective Mean Stress $(\sigma_1 + 2\sigma_3)/3$-P_p
PA Tuff (Tufo del Palatino Unit)							
T0_PA	1.54	33.39[a]		-	-	-	-
Twh1_PA	1.55	31.8	110	-	-	-	$P^* = 41$
Twh2_PA	1.51	36.1	110	-	-	-	$P^* = 35$
Tw1_PA	1.58	31.8	5	-	-	27.9	14.0
Tw2_PA	1.57	31.3	10	-	-	28.8	19.9
Tw3_PA	1.57	31.8	20	-	-	24.2	28.1
Tw4_PA	1.56	32.7	30	-	-	18.1	36.2
Tdu_PA	1.57	32.15[a]	0	33.4	12.1	-	-
Tdh_PA	1.54	32.6	130	-	-	-	$P^* = 60$
Td1_PA	1.56	32.69[a]	5	48.4	21.5	-	-
Td2_PA	1.56	32.65[a]	30	-	-	34.2	42.7
Td3_PA	1.56	32.58[a]	45	-	-	23.2	53.0
PI Tuff (Tufo Pisolitico di Trigoria Unit)							
T0_PI	1.50	36.74[a]	0	-	-	-	-
Twh_PI	1.51	35.0	40	-	-	-	$P^* = 28$
Tdh_PI	1.53	35.45[a]					$P^* = 56$
Tdu_PI	1.50	36.84[a]	0	17.4	5.8	-	-
Td1_PI	1.63	31.22[b]	5	42.9	19.3	-	-
Td2_PI	1.74	26.75[b]	10			25	45.04
Td3_PI	1.52	36[a]	30	-		29.5	39.89
Td4_PI	1.50	38.6	45	-		18.8	51.28

[a]Porosity inferred from grain density values, 2.31 and 2.37 for PA and PI, respectively.
[b]Samples with denser zones.

The porosity change was calculated from the ratio of the pore volume change to the initial bulk volume of the sample. The displacement was measured outside the pressure vessel with a DCDT mounted between the moving piston and the fixed upper platen. For dry experiments, the volumetric strain was calculated using the relation $\varepsilon_V = \varepsilon_{\|} + 2\varepsilon_{\perp}$, where $\varepsilon_{\|}$ and $\varepsilon_{\perp}$ are the strains measured in the axial and transverse directions, respectively.

[16] The load, displacement, and strain gage signals were acquired by a 16-bit A/D converter at a sampling rate of 1 s^{-1} with resolutions of 0.3 MPa, 1 μm and 10^{-5}, respectively. Uncertainty in strain was estimated to be 2×10^{-4} (when calculated from the DCDT signal) and 10^{-5} (when measured directly by the strain gages). Acoustic emission activity can be monitored by the piezoelectric transducer attached to the sample. However, since the activity in our tuff samples was not significant, we did not use any of the acoustic emission data in this study.

2.4. Microstructural Analysis

[17] Microstructure of the two undeformed and seven deformed samples was studied under optical microscope and scanning electron microscopes (SEM) on thin sections. Optical microscopy was performed using a Nikon optical polarizing microscope. For SEM observations, the gold-coated thin sections were studied at Stony Brook using a LEO 1550 microscope with a voltage up to 10 KV. Additional observations on the undeformed samples were performed at INGV Rome using a JEOL JSM-6500F thermal field emission SEM. All SEM micrographs presented here were acquired in the backscattered electron mode.

[18] To characterize the pore size statistics of an undeformed tuff sample, the thin section of T0_PA (from the Tufo del Palatino block) was scanned using an Epson Perfection™ V700 photo scanner at a resolution of 3200 dpi. Our experience has been that the scanner can resolve the macroporosity as effectively as an optical microscope, with the advantage that it can cover the whole area of the thin section, thus circumventing the need to assemble a mosaic of numerous optical micrographs [*Zhu et al.*, 2010]. The macropores were identified using a brightness (gray scale) thresholding approach [*Russ*, 1990], and the binarized image was then analyzed using ImageJ, a public domain image processing program developed at the National Institute of Health. The area of each individual pore was determined, and the equivalent diameter of a circle with the same area was evaluated.

3. Mechanical Data

[19] Table 1 summarizes the deformation history of all tuff samples in this study. The convention is adopted that compressive stresses and compactive strains (i.e., shortening and porosity decrease) are positive. The maximum and

minimum principal stresses will be denoted by σ_1 and σ_3, respectively. The dry and wet experiments are denoted by the letters "Td" and "Tw," respectively. Hence, Td2_PI corresponds to number 2 of a series of four triaxial compression experiments on nominally dry samples of the Tufo Pisolitico block. The letter "u" and "h" indicate uniaxial compression and hydrostatic tests, respectively. Hence, Twh1_PA corresponds to the first of two hydrostatic compression tests on saturated samples of the Tufo del Palatino block.

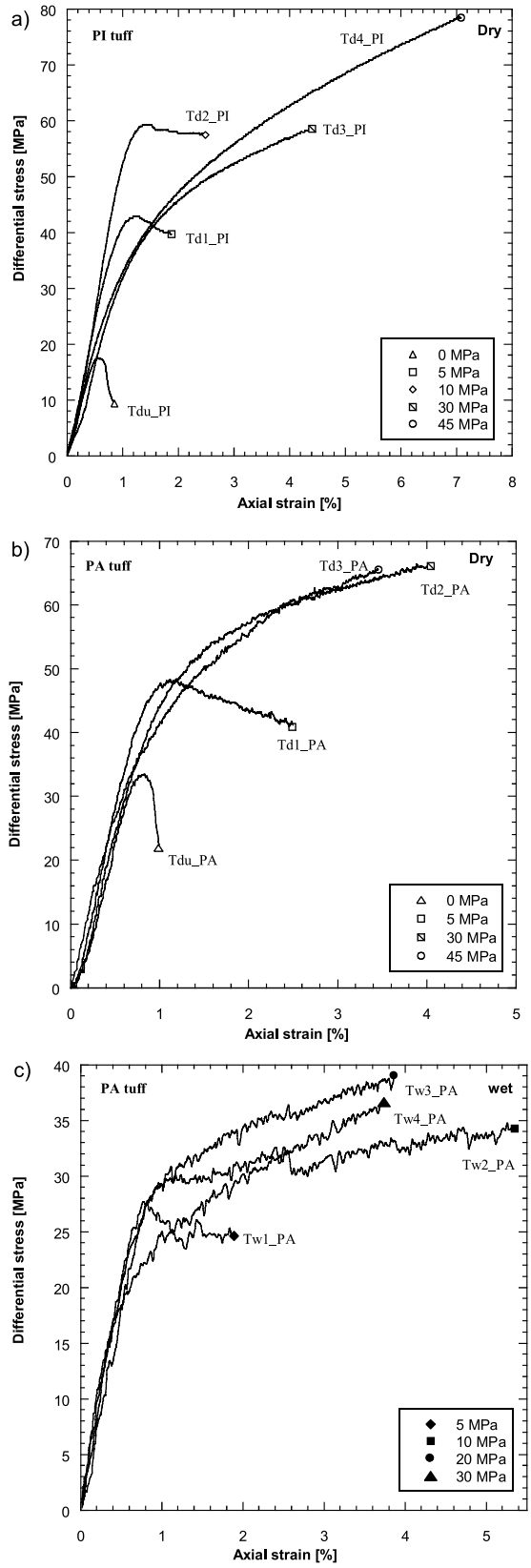

Figure 2. Stress-strain curves of (a) dry PI tuff (Tufo Pisolitico) with confining pressures ranging from 0 MPa to 45 MPa; (b) dry PA tuff (Tufo de Palatino) with confining pressures ranging from 0 MPa to 45 MPa, and (c) wet PA tuff (Tufo de Palatino) with effective pressures ranging from 5 MPa to 30 MPa. The samples corresponding to each curve are denoted in the plot, with symbols representing the effective pressures.

[20] The brittle-ductile transition in a porous ignimbrite is illustrated by the mechanical data for dry Tufo Pisolitico samples at confining pressure ranging from room pressure to 45 MPa (Figure 2a). In uniaxial compression, the sample Tdu_PI attained a peak stress and then failed by strain softening. At a confining pressure of 5 MPa, the sample Td1_PI attained a peak stress significantly higher than the uniaxial compressive strength, after which it strain softened and the stress dropped stably to attain a residual level. This sample failed by development of a shear bands oriented at ~30° to σ_1. At confining pressure of 10 MPa, the sample Td2_PI attained a peak stress and quickly decayed to a plateau. At more elevated pressures, the samples Td3_PI and Td4_PI both showed strain hardening, with differential stress increasing monotonically with increasing strain. Strain localization was not observed, after unloading, in these samples that failed by cataclastic flow.

[21] The mechanical data and failure modes for dry samples from the Tufo del Palatino block are qualitatively similar (Figure 2b), but probably due to the lower porosities, the stresses involved were higher than those for corresponding experiments on Tufo Pisolitico (Figure 2a).

[22] Mechanical data for saturated samples of Tufo del Palatino (Figure 2c) indicated significant weakening of the porous tuffs in the presence of water. At an effective pressure (confining pressure minus pore pressure) of 5 MPa, the peak stress (near the plateau) was about half of that for a dry sample that failed by brittle faulting. Strain localization was not obvious in the failed sample Tw1_PA, implying that the brittle-ductile transition in a wet sample would occur at a lower effective pressure. The significant water-weakening effect we observed in the Alban Hills tuffs is comparable to that reported in previous studies on tuffs from Yucca Mountain [*Martin et al.*, 1994, 1995].

[23] To illustrate the development of inelastic volume change, we show in Figure 3 data for the development of mean stress $(\sigma_1 + 2\sigma_3)/3$ and effective mean stress (mean stress minus pore pressure) with volumetric strain for the Tufo del Palatino samples. The triaxial and hydrostatic compression data are shown as solid and dashed curves, respectively. On each of the hydrostats, an approximately linear poroelastic stage is first observed. A significant deviation from poroelasticity can then be identified in each of the hydrostats from a point marked by P^* (Figures 3a and 3b), which is interpreted to be associated with the onset of pore collapse analogous to hydrostatic compres-

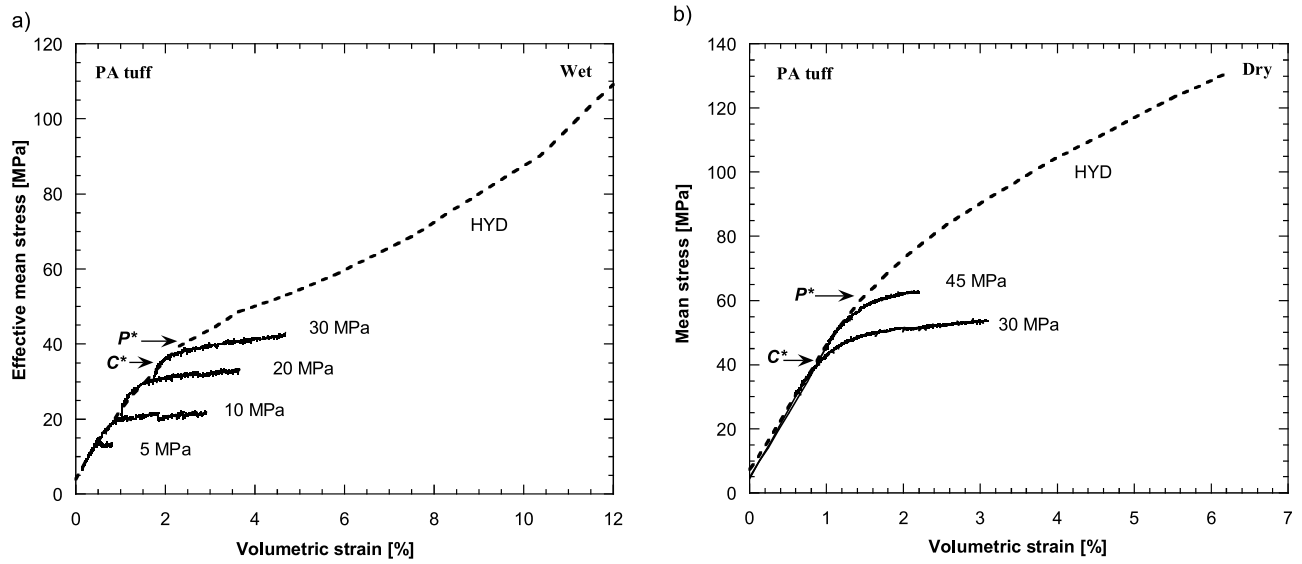

Figure 3. Volumetric strain versus mean stress for triaxial compression experiments on (a) wet PA tuff (Tufo de Palatine), and (b) dry PA tuff. For reference, the hydrostatic data are shown as the dashed curve. Numbers next to each curve indicate the effective pressures maintained during the experiments. The critical pore collapse pressure P^* and the onset of shear-enhanced compaction C^* at effective pressure of 30 MPa are marked by arrows.

sion behavior in porous sandstones [*Zhang et al.*, 1990] and carbonate rocks [*Vajdova et al.*, 2004]. In the cataclastic flow regime, the triaxial compression curve for a given effective pressure basically coincided with the hydrostat up to a critical stress state C^* (as indicated in Figures 3a and 3b for the experiment at 30 MPa effective pressure), beyond which there was an accelerated increase in porosity reduction in comparison to the hydrostat. This implies that the deviatoric stress field provided significant inelastic contribution to the compactive strain, a phenomenon called "shear-enhanced compaction" that initiated at yield stress level C^* [*Wong et al.*, 1997]. Our data for Tufo del Palatino show lower values for the critical pressure P^* for onset of pore collapse and critical stress C^* for onset of shear-enhanced compaction were observed in the presence of water.

4. Microstructural Observations

[24] Observed under the optical microscope, our undeformed Alban Hills tuffs include a small number of lithic clasts and pumices (up to cm in scale) embedded in a fine-grained glassy matrix. Figure 4a shows one such pumice containing numerous relatively large pores. Figure 4b shows the interior of a lapilli with lower degree of vesculation, which should probably be classified as a scoria. Figure 4c shows a shard with relatively straight edges and sharp corners, characteristic of an ignimbrite that is nonwelded. Figure 4d shows another scoria clast, containing numerous pores with dimensions up to 100 μm.

4.1. Macropores, Micropores, and Microcracks

[25] We observed equant pores of many different scales as well as complex networks of fine microcracks in the Alban Hills tuff samples. Figure 4e shows an area in the matrix with large pores (~100 μm) and many smaller ones (~10 μm), and Figure 4f shows another area with pores mostly in the 10 μm range. However, when we zoomed into the subarea inside the white dashed rectangle, we were able to resolve numerous μm-sized pores. Furthermore we also observed a complicated complex of elongated microcracks with different degrees of connectivity. While some appear to have been healed, many of the microcracks seem open with a finite aperture.

[26] To characterize the partitioning of porosity among these features, we followed the approach of *Zhu et al.* [2010] to evaluate the macroporosity (defined here to be that part of the total porosity associated with equant pores with equivalent diameter >33 μm, limit corresponding to the thickness of our thin sections) by analyzing a scanned image of the thin section T0_PA. In Figure 5a we show a binarized image of an area of this sample scanned at 3200 dpi. Porosity is shown as dark areas (with very low brightness level). There are isolated areas with irregular shape that could be grains plucked out during the preparation of thin section. Using the ImageJ software, area of each individual pore was determined, and the equivalent diameter of a circle with the same area was evaluated. At 3200 dpi, the pixel size of the scanned image is less than 10 μm. Since the resolution of such observations on a petrographic thin section is conventionally taken to be limited by its thickness (~33 μm), we only included those pores with equivalent diameter >33 μm in the histogram shown in Figure 5b. The size distribution of macropores ranges over one order of magnitude, with a maximum diameter of 794 μm. The areal macroporosity evaluated from our binarized image is 11.7% for our Alban Hills tuff, which is about 1/3 the total porosity of 32% (Table 1). This represents an upper

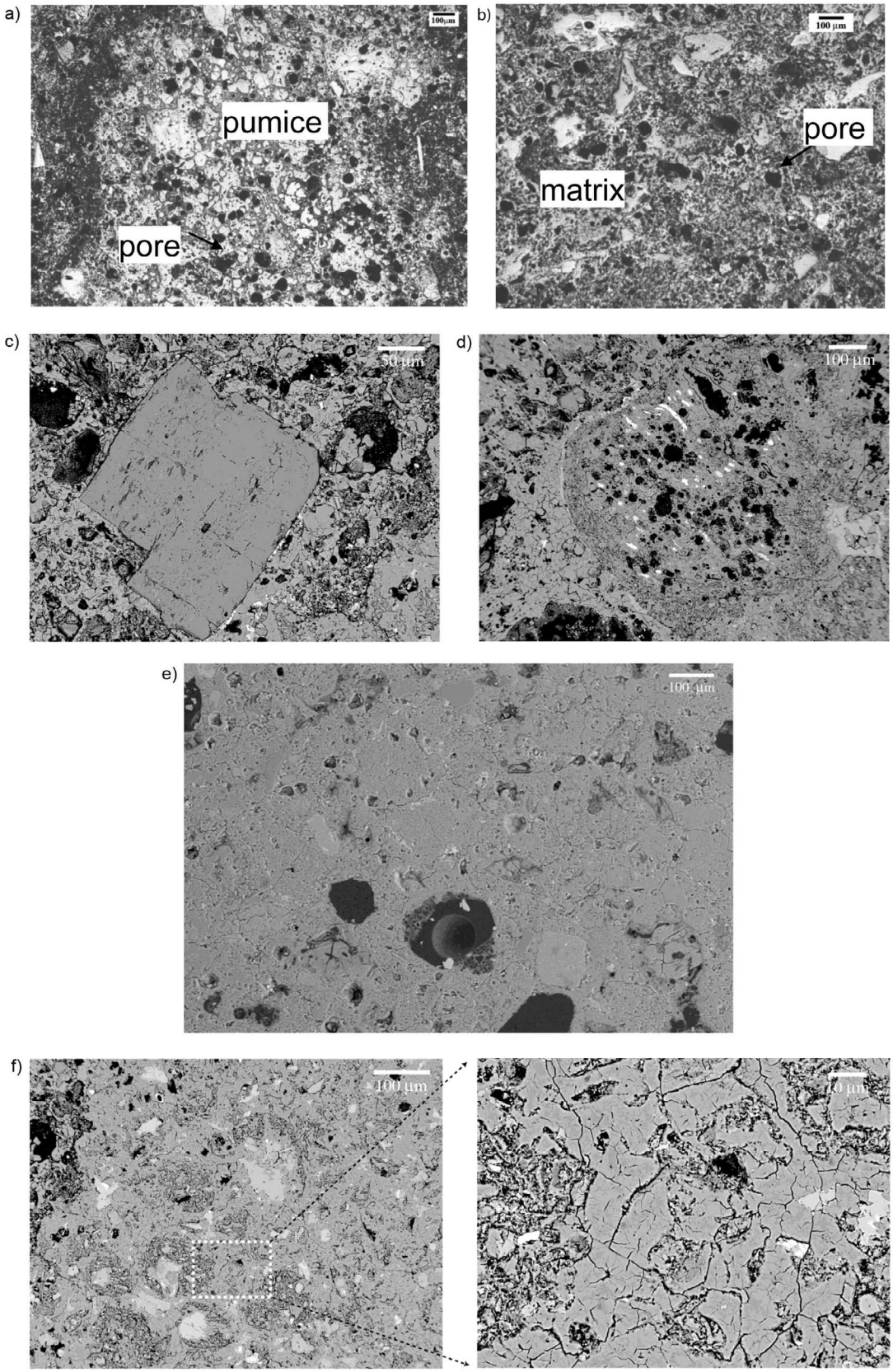

Figure 4

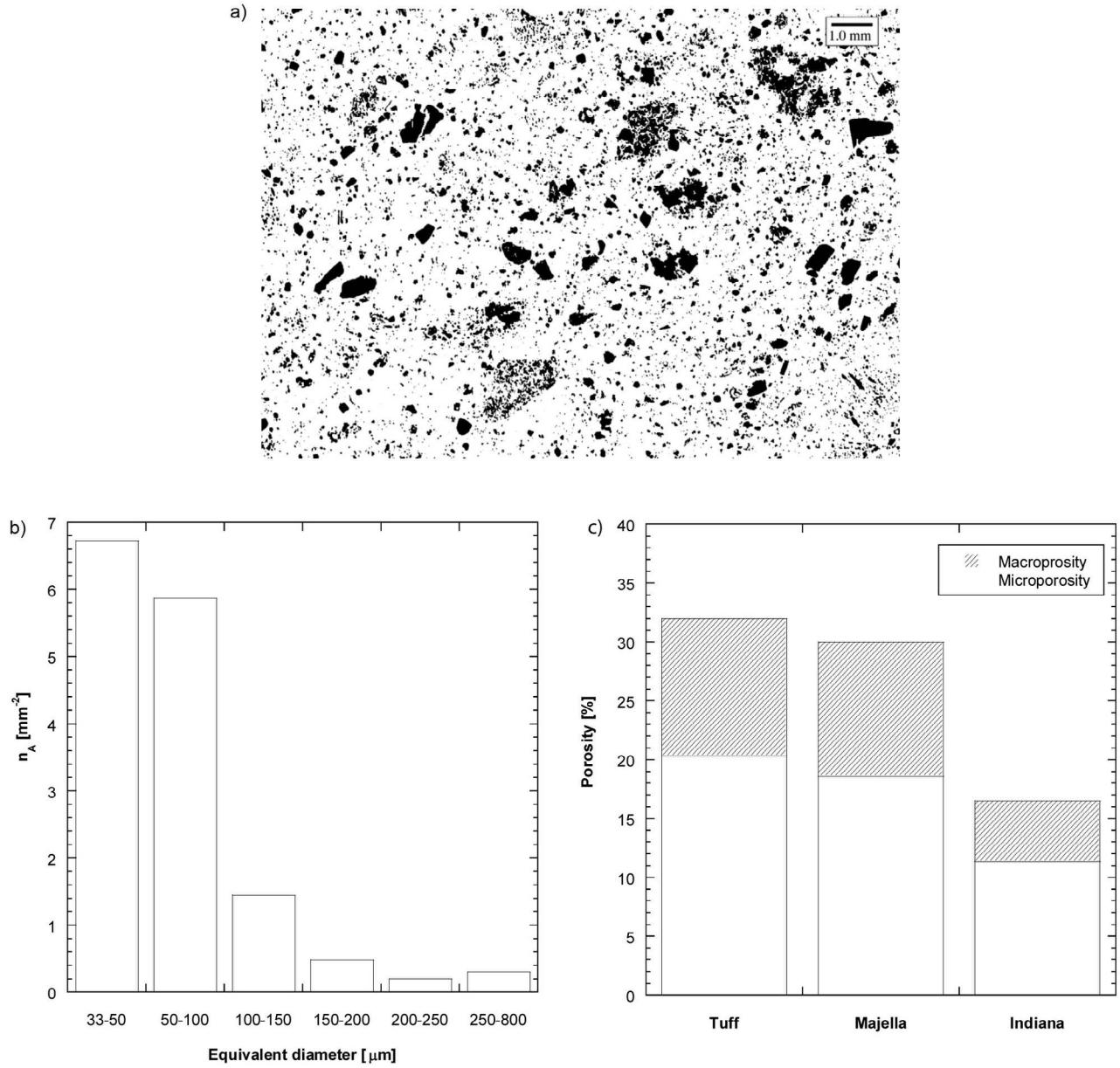

Figure 5. (a) Binarized image of intact Alban Hills tuff sample. Macropores resolved under optical microscope are shown in black. Isolated area with irregular shape could be plucked out grains. (b) Size distribution of pores in an undeformed Alban Hills tuff sample that can be resolved under optical microscope. The number of pores per unit area is plotted versus equivalent diameter. Only data for diameters greater than 33 μm are shown. (c) Partitioning of microporosity and macroporosity in Alban Hills tuff. For comparison, histograms of Majella and Indiana limestones [*Zhu et al.*, 2010] are also shown.

bound, since it may include areas associated with plucked grains.

[27] We define "microporosity" to be the difference between total porosity and macroporosity. Figure 5c summarizes the partitioning between macroporosity and microporosity in our tuff sample, and for comparison values for two limestones determined by *Zhu et al.* [2010] using an identical approach. Our data show that the porosity parti-

Figure 4. Micrographs of intact Alban Hills tuff sample. (a) A pumice and (b) interior of a lapilli observed under optical microscope. Pores are represented by the dark areas as marked in the image. Backscattered FESEM images of (c) a relatively intact shard with straight edges and sharp corners, and (d) a scoria clast in an undeformed Alban Hills tuff. Pores with dimensions up to 100 μm are shown as black areas. (e) Backscattered SEM images of large pores (~100 μm) and smaller pores (~10 μm) embedded in tuff matrix. (f) Backscattered FESEM images of smaller pores on the order of 10 μm embedded in matrix. Numerous μm-sized pores and elongated microcracks were observed in the zoomed-in image on the right.

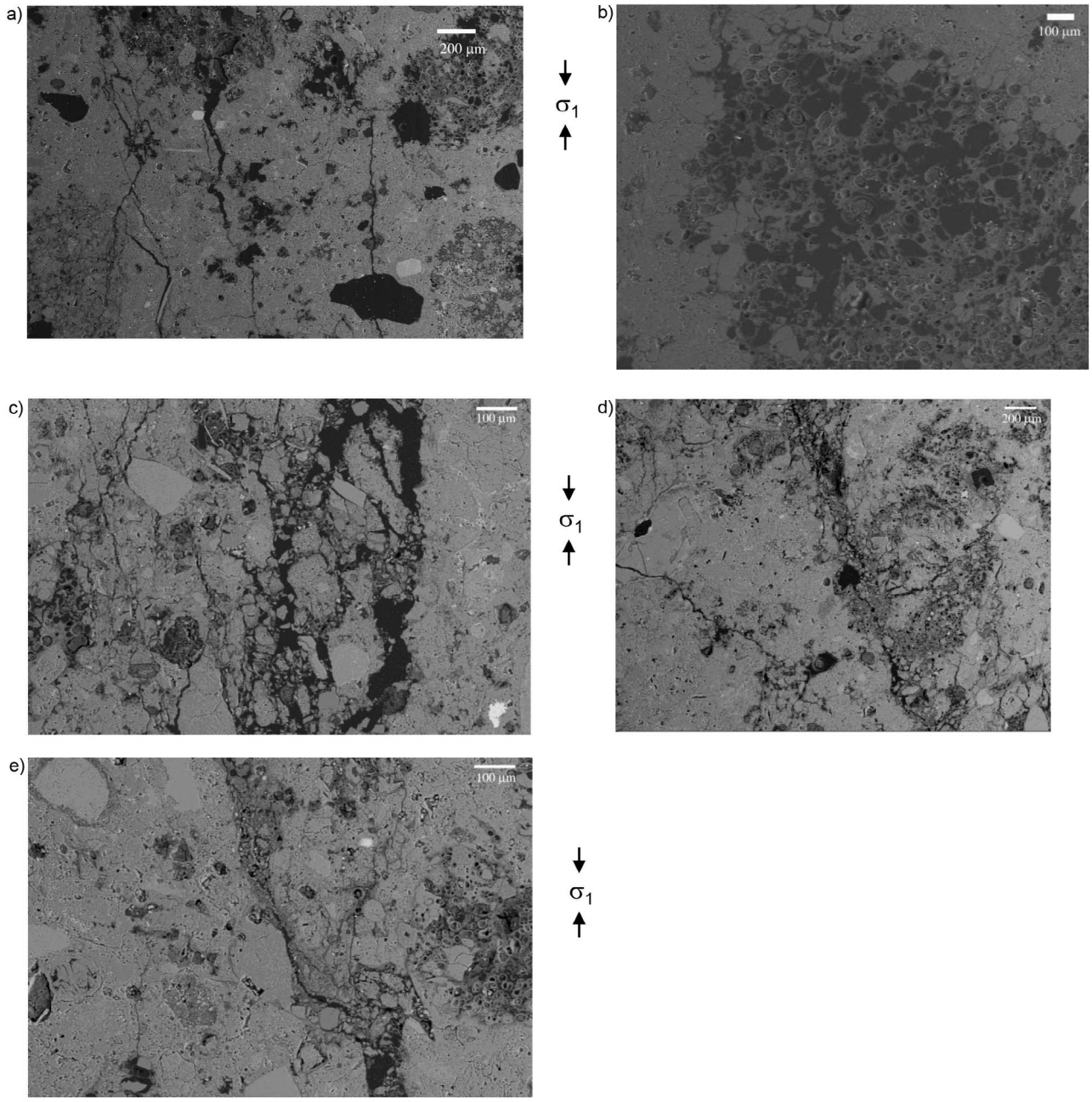

Figure 6. Backscattered SEM images of Alban Hills tuff samples failed in brittle regime. Direction of σ_1 is vertical. (a) Sample Tdu_PA that failed in uniaxial compression. Stress-induced microcracks were observed to emanate from relatively large pores in matrix and propagated subparallel to σ_1. (b) A pumice in sample Tdu_PA. Macropores embedded in the pumice were not observed to interact with wing cracks. (c) Sample Td1_PA loaded to post peak. Intense microcracking and comminution were observed in the vicinity of the shear band. (d) A macropore embedded in matrix of sample Tdu_PA. Numerous stress-induced cracks subparallel to σ_1 had emanated from the macropore and coalesced with each other. (e) A path along which shear localization had developed in sample Tdu_PA. The development was observed to bypass the lithic clasts by traversing along their boundaries.

tioning in Alban Hills tuff is very similar to that in the two limestones, in which the microporosity represents a very significant fraction of the total porosity. The ratio between microporosity and total porosity has values of 0.63, 0.62 and 0.68 for Tufo del Palatino, Majella limestone and Indiana limestone, respectively.

[28] In spite of this similarity, there is a qualitative difference in the microporosity in tuff and limestone, in

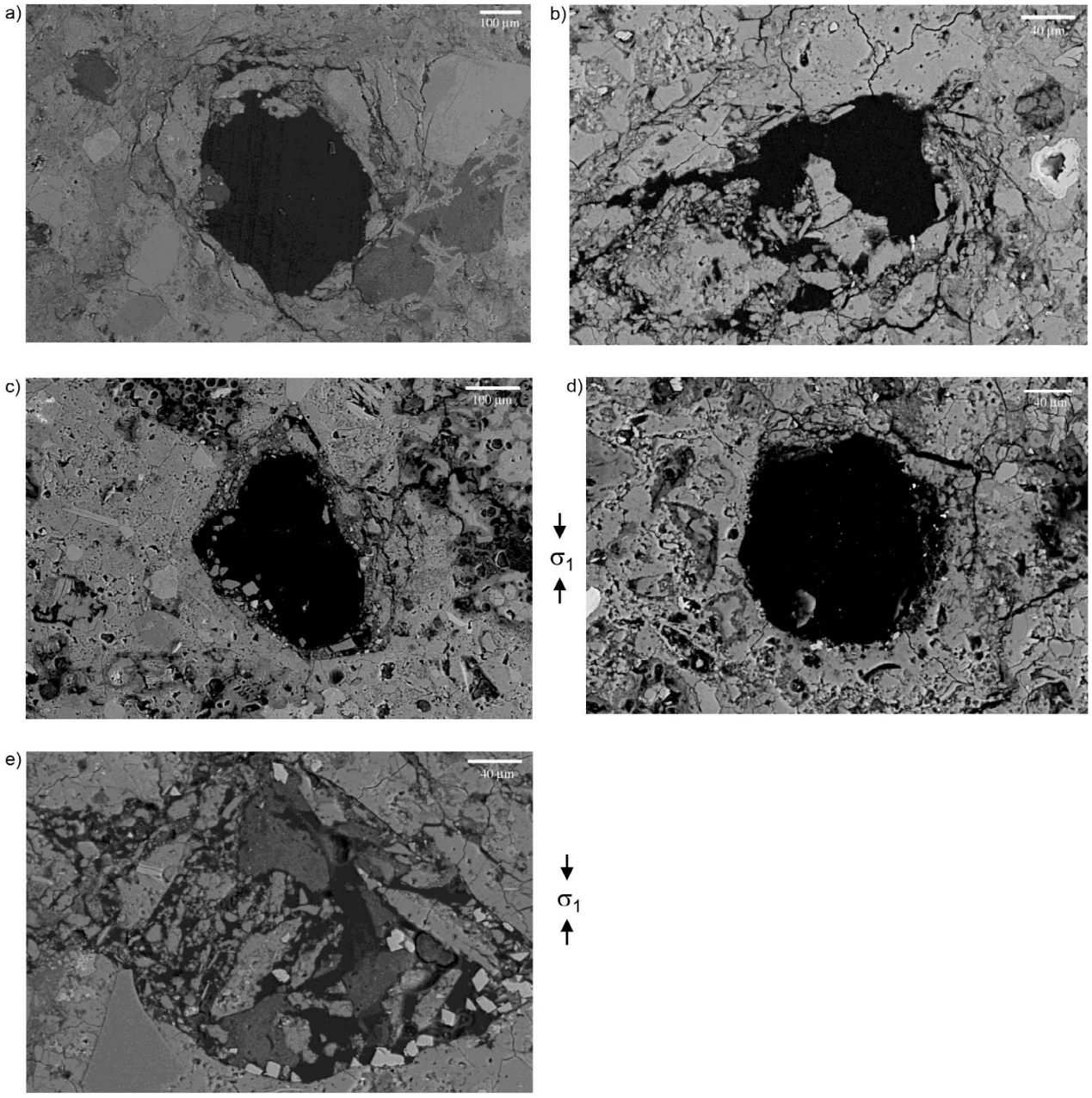

Figure 7. Backscatter SEM images of Alban Hills tuff samples failed by inelastic compaction. (a) Sample Twh1_PA was hydrostatically compacted beyond the critical pore collapse pressure P^*. A macropore in matrix surrounded by intensive cataclastic damage was observed. The damage zone had extended a distance ~100 μm. (b) A collapsed pore in matrix in sample Twh1_PA. The micropore, with a diameter ~60 μm, was about 5 times smaller than the macropore in Figure 7a. Stress-induced cracks had coalesced around the pore surface. (c) Sample Tw4_PA was stressed to beyond the compactive yield stress C^*. A macropore in matrix with a diameter ~250 μm was observed to collapse. A thin layer of crushed grains in the periphery of the macropore was formed by the propagation and coalescence of stress-induced microcracks. (d) A collapsed micropore with a diameter of ~90 μm in sample Tw4_PA. Microcracks had emanated from the micropore and coalesced around the pore circumference. (e) Collapse of spalled fragments into a macropore in sample Tw4_PA. Crushed grains had fallen into the interior of the macropore.

that the former includes a very significant number of microcracks (Figure 4f). However, since microcrack porosity depends not only on the number but also the aperture, a dense population of microcracks typically contributes very little toward the porosity. Accordingly the microporosity inferred from our measurements is expected to derive mostly from equant micropores (Figures 4e and 4f).

4.2. Brittle Faulting

[29] The uniaxially compressed samples Tdu_PA and Tdu_PI both failed by the development of a throughgoing shear band at ~30° with respect to σ_1. In the failed sample Tdu_PA, we observed a shear zone ~0.1 mm wide. Stress-induced microcracks subparallel to were observed to have emanated from relatively large pores embedded in the matrix (Figure 6a). In contrast, such wing cracks were not observed in relation to macropores in a pumice (Figure 6b).

[30] The sample Td1_PA failed in the brittle faulting regime (Figure 2b). Intense microcracking had developed in the vicinity of the shear bands that had developed in the failed sample (Figure 6c). Numerous stress-induced cracks subparallel to σ_1 had coalesced. Figure 6d shows a macropore embedded in the matrix, with numerous microcracks aligned subparallel to that had emanated from the macropore and coalesced with each other. Figure 6e shows the path along which shear localization had developed, which seems to have bypassed the lithic clasts by traversing along their boundaries. A similar observation was reported by *Evans and Bradbury* [2004], who found in naturally deformed samples of the Bishop tuff that the fracture paths seem to lie preferentially along the boundaries of phenocrysts, lapilli and lithic clasts.

4.3. Inelastic Compaction

[31] Damage in the inelastically compacted samples is primarily associated with pore collapse. The sample Twh1_PA was hydrostatically compressed to an additional 70 MPa beyond the critical pressure P^* (Figure 3a). Macropores at various stages of collapse were observed in this sample. It should be noted that for such a relatively weak pyroclastic rock, it is unavoidable that some grains would be plucked out when one prepares a thin section. Hence, care should be taken not to interpret by mistake such a plucked grain as a collapsed pore, which should retain fragments either attached to the pore periphery or spalled into the pore interior.

[32] We show in Figure 7a the collapse of a macropore in matrix with a diameter of ~300 μm. Intensive cataclastic damage was observed near the surface with numerous microcracks surrounding the macropore. Pore-emanated cracks have extended a distance around 100 μm. The area beyond the damage zone seems to be relatively undeformed. Figure 7b shows a collapsed pore in the matrix with a diameter around 60 μm. The micropore observed is about 5 times smaller than the macropore. Stress-induced microcracks coalesced around the pore surface. The intensive damage zone has propagated radially by ~50 μm.

[33] The sample Tw4_PA was triaxially compressed to beyond the compactive yield stress C^* at a confining pressure of 30 MPa (Figure 3a). The development of shear-enhanced compaction was manifested by pervasive collapse of macropores. We show in Figure 7c a collapsed macropore within the matrix with a diameter of ~250 μm. Intensive damage was observed around the pore surface. Stress-induced microcracks had extended and coalesced with each other, which led to a thin layer of crushed grains in the periphery of the macropore. The damage zone has extended radially by ~60 μm and the area beyond remained intact. Besides macropores, collapse of some of the larger micropores was also observed in the triaxially compacted sample. Figure 7d shows a micropore with a diameter of ~90 μm. Microcracks had emanated from the micropore and coalesced around the pore circumference. In Figure 7e we show the cataclastic damage of pore collapse in sample Tw4_PA. Crushed grains had spalled and fallen into the interior of the macropore while the matrix seems relatively undeformed.

5. Discussion

[34] The development of dilatancy and micromechanics of brittle faulting in compact crystalline rocks and porous siliciclastic rocks have been extensively investigated [*Paterson and Wong*, 2005]. Our observations here have shown that the brittle faulting processes in a porous tuff are similar in many respects. Shear localization does not develop until the postfailure stage after the peak stress has been attained. The postpeak deformation is stabilized by increasing pressure. The tuff contains numerous preexisting microcracks which can readily nucleate stress-induced damage. Very high density of microcracking is observed within the shear zones.

[35] However, there seem to be at least two important differences. First, the pore space in our Alban Hills tuff has numerous pores which, according to our microstructural observations, assume a significant role in the nucleation of stress-induced microcracks. In this respect, it is somewhat similar to recent observations in porous limestones [*Zhu et al.*, 2010; *Vajdova et al.*, 2010], in which a key mechanism for brittle faulting is pore-emanated cracking. Second, the water-weakening we observed here for Alban Hills tuffs (Table 1) and *Martin et al.* [1994, 1995] reported for Yucca Mountain tuffs is significantly stronger than that observed in a siliciclastic rock or compact crystalline rock [*Baud et al.*, 2000a; *Paterson and Wong*, 2005].

[36] As for inelastic compaction and cataclastic flow, our observations indicate that the phenomenology in a porous tuff is qualitatively similar to that in a siliciclastic [*Wong et al.*, 1997] or carbonate [*Vajdova et al.*, 2004] rock. Notwithstanding these similarities, our observations also underscore that the micromechanics in tuff is very different from that in a clastic rock such as sandstone, which involves primarily grain crushing initiated by the stress concentrations at grain contacts [*Menéndez et al.*, 1996]. In some respects, the behavior in tuff is qualitatively similar to that documented recently in porous limestones [*Zhu et al.*, 2010; *Vajdova et al.*, 2010], which typically involves pore collapse that initiates from stress concentrations at the periphery of the larger pores. Similar partitioning between macroporosity and microporosity was also observed (Figure 5c). Given these apparent similarities, a first question we would like to address is whether and to what extent the micromechanical models formulated for a porous limestone can be extended to a porous tuff. This requires a synthesis of our mechanical data with other published data.

5.1. Uniaxial Compressive Strength of Nonwelded and Welded Tuffs

5.1.1. Welded Tuff

[37] Previous rock mechanics studies of tuff have mostly focused on the uniaxial compressive strength (UCS) as a

geotechnical property. In particular, tuff samples from both outcrops and boreholes in Yucca Mountain, Nevada have been investigated extensively [*Nimick et al.*, 1985; *Martin et al.*, 1994, 1995; *Schultz and Li*, 1995; *Lockner and Morrow*, 2008; *Avar and Hudyma*, 2007]. The porosity of 198 samples of ignimbrites from three boreholes at Yucca Mountain ranges from as low as 1% in the densely welded tuffs to 53% in the zeolitized nonwelded tuffs [*Nelson and Anderson*, 1992]. The two primary units at the proposed repository site are Paintbrush and Calico Hills. The former unit has a wide range of welding characteristics (from nonwelded to densely welded), and the comprehensive investigations of *Martin et al.* [1994, 1995] concluded that no apparent correlations between porosity and the UCS were observed on welded Paintbrush tuff. A similar conclusion was reached by *Mogi* [1964] who investigated three welded tuffs from Japan, and by *Moon* [1993a, 1993b] who investigated a large variety of ignimbrites from New Zealand.

[38] We compiled UCS data on welded tuff are plotted them versus total porosity in Figure 8a. At a given porosity, the UCS has been observed to vary by as much as one order of magnitude. It is possible that welding of the highly plastic glass shards induced by heat and overburden could result in significant geometric complexity in the pore space, such that the mechanical behavior is controlled by not only the porosity but also other microstructural attributes. Indeed it has been suggested that attributes including the nature of welding, microcrack density, as well as the presence of lithophysae, pumice and clay minerals all exert important influence on the strength of a welded tuff [*Price and Bauer*, 1985; *Moon*, 1993a; *Avar and Hudyma*, 2007]. Deeper understanding of this question would require a systematic investigation of the mechanics of failure in welder tuffs, which should be pursued in future investigations even though it is beyond the scope of the present study.

5.1.2. Nonwelded Tuff

[39] Laboratory studies have shown an overall trend for nonwelded tuffs to be weaker and less brittle than welded tuffs. Field observations have also indicated that degree of welding influences the dominant deformation mechanisms in different ignimbrites. Whereas highly localized and closely spaced fractures embedded in a damage zone are often observed in a highly to moderately welded ignimbrite, diffuse arrays of deformation bands typically develop in poorly welded units [*Wilson et al.*, 2003; *Evans and Bradbury*, 2004; *Riley et al.*, 2010]. We compiled in Figure 8b the UCS data for nonwelded tuffs with porosities ranging from 0.3% to 57.1%. Our Tufo Pisolitico and Tufo del Palatino samples are considered to be nonwelded. In Yucca Mountain, the tuff from the Calico Hills unit is also classified as nonwelded ignimbrites [*Schultz and Li*, 1995; *Lockner and Morrow*, 2008]. Ignimbrites retrieved from three boreholes (USW G-4, NRG-6 and NRG7/7a) that penetrated the Paintbrush tuff (which overlies the Calico Hills formation) showed different degrees of welding [*Nimick et al.*, 1985; *Martin et al.*, 1994, 1995]. Only data for the nonwelded Paintbrush tuff samples are shown in Figure 8b. We also included the data of *Aversa and Evangelista* [1998] for the Neapolitan fine-grained tuff, a highly porous ignimbrite deposited in the Phlegrean Fields (Campi Flegrei) in Naples.

[40] The tuffs from Alban Hills, Yucca Mountain and Phlegrean Fields all have porosities >10%. We were able to locate two sets of data for relatively compact, nonwelded tuffs from Hong Kong with porosities <10%. The most compact samples (with porosities down to 0.3%) were from the Tuen Mun Formation, described as a tuff breccia that contains "subrounded to angular fragments of marble, quartzite and metasandstone embedded in a greenish grey to grey fine-grained tuff matrix" [*Hong Kong Geotechnical Control Office*, 1990]. Given their relatively low porosities, one may have expected these tuffs to be welded. However, comparison with strength data for welded tuffs in the low porosity range (Figure 8a) indicates that indeed the Tuen Mun tuffs tend to have lower UCS. In addition, *Dobson and Nakagawa* [2005] investigated 4 samples from the Aberdeen Tunnel of Hong Kong. According to their petrographic observations, the rock is a rhyolitic tuff that contains broken phenocrysts of quartz and feldspar in a devitrified, microcrystalline groundmass.

[41] There is an overall trend for the saturated samples to be appreciably weaker (Figure 8b), a phenomenon possibly related to the weakening in the presence of water which we will discuss in a latter section. Given the diversity of pyroclastic and volcanoclastic processes involved in the formation of these nonwelded tuffs, it is surprising that their UCS data show a rather systematic correlation with the total porosity. In light of this apparent correlation and our microstructural observations, we will first attempt to interpret this trend using the pore-emanated cracking model of *Sammis and Ashby* [1986], which would predict a one-to-one correspondence between UCS and porosity for rocks with similar pore sizes. The two-dimensional damage mechanics model considers an elastic medium pervaded by circular holes of uniform radius r. As the applied stress increases, a point is reached when the stress intensity factor of a small crack on the circular surface attains the critical value K_{IC}, at which point extensile cracks would initiate from the poles and propagate to a certain distance parallel to the σ_1 direction. As the stress-induced cracks propagate to longer distances with increasing stress, they interact with one another to induce an additional tensile stress intensity, ultimately leading to an instability with coalescence of the pore-emanated cracks at the peak stress level.

[42] At a fixed lateral stress, *Sammis and Ashby*'s [1986] pore-emanated cracking model for brittle failure predicts that the peak differential stress scales with the parameter $K_{IC}/\sqrt{\pi r}$. For uniaxial compression, *Zhu et al.* [2010] have recently obtained an analytic estimate of the UCS σ_u as a function of porosity Φ:

$$\sigma_u = \frac{1.325}{\Phi^{0.414}} \frac{K_{IC}}{\sqrt{\pi r}} \tag{1}$$

We compare in Figure 8b this analytic approximation with our compiled UCS data for nonwelded tuff. Except for some extremely weak tuffs at the high porosity end, most of the data can be bracketed by the two theoretical curves corresponding to $K_{IC}/\sqrt{\pi r} = 5$ and 35 MPa. If the pore-emanated cracking initiates intragranularly within a lithic clast, an estimate of K_{IC} can be made based on experimental measurements on common silicate minerals. For feldspars, the measured values are ~0.3 MPa $m^{1/2}$ and can be higher (but not by order of magnitude) in other silicate minerals such as quartz and olivine. In a glass experimental measurements of

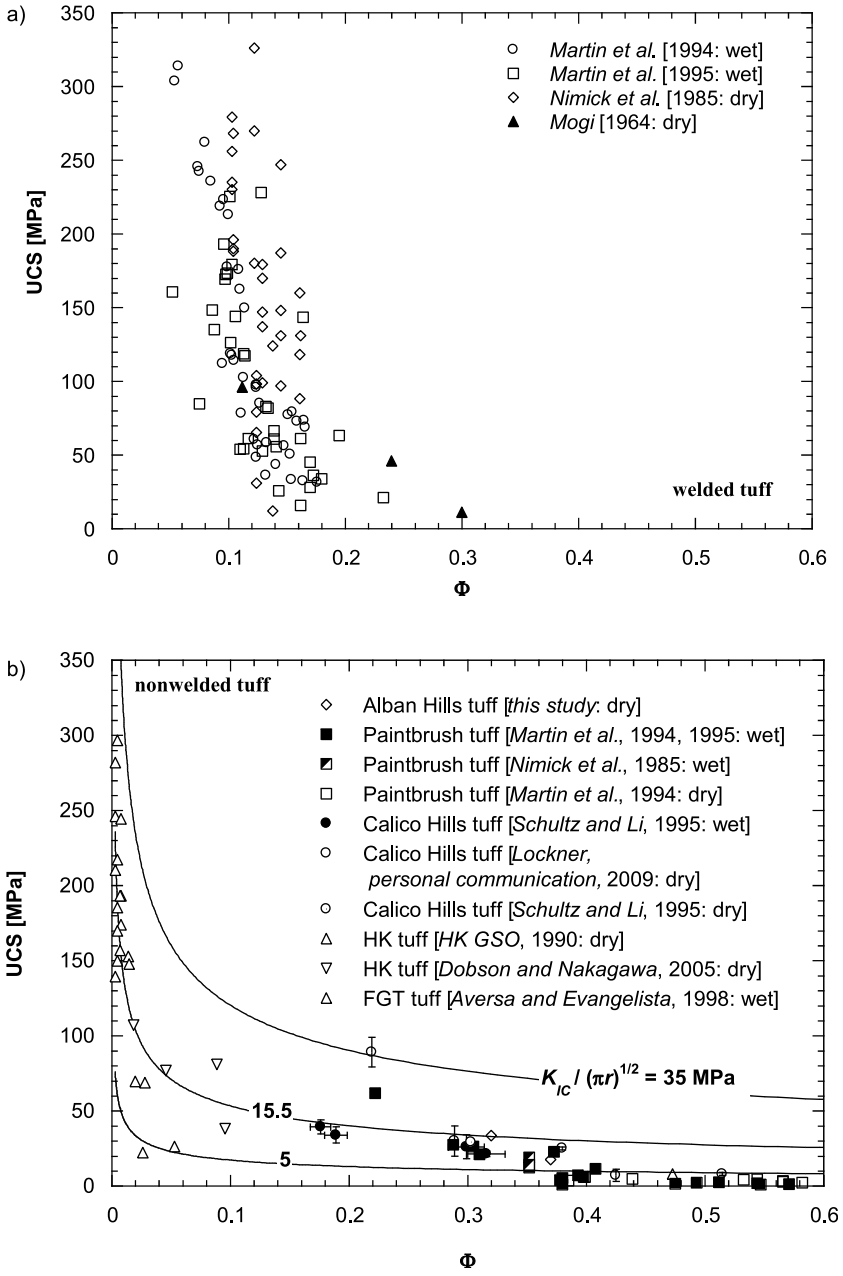

Figure 8. Compiled uniaxial compressive strength (UCS) data are plotted as a function of total porosity. (a) Experimental data of welded tuffs from Yucca Mountain and Japan are shown by open and solid symbols, respectively. No apparent correlations were observed between UCS and porosity for the welded tuffs. (b) Comparison of theoretical predictions with laboratory data on UCS of nonwelded tuff samples. Theoretical curves of UCS as a function of total porosity for three different values of $K_{IC}/\sqrt{\pi r}$ are plotted. Most of the data can be bracketed by two limiting curves with $K_{IC}/\sqrt{\pi r}$ = 5 and 35 MPa. The standard deviations of data on Calico Hills tuff are represented by error bars.

K_{IC} are also higher. However, if the wing crack grows along a grain boundary (along scoria or lithic clasts), K_{IC} is expected to be lower, possibly by a factor of 2 or so [*Atkinson and Meredith*, 1987]. As elaborated in a latter section, its value is also expected to be lower in the presence of water.

[43] If we were to assume K_{IC} = 0.3 MPa $m^{1/2}$, then according to equation (1) the laboratory data for UCS of nonwelded tuffs are bracketed by average macropore size ranging from r = 23 μm to 1.15 mm. Specific to our Tufo del Palatino sample (Tdu_PA), the inferred pore diameter is $2r$ = 238 μm, which is comparable to our microstructural observations on the macropore size (Figure 4e). This indicates that it is viable for the larger pores in the tuff to provide stress concentration sites for wing cracks to initiate and coalesce, leading to brittle failure as analyzed in the damage mechanics model of *Sammis and Ashby* [1986].

[44] However, it should be noted that the Tufo Pisolitico sample (Tdu_PI) has a UCS which is about half that of Tdu_PA (Table 1), which would imply an average pore diameter of ~780 μm using the same K_{IC} value. This inferred diameter is larger than most of what we observed under the microscope, and the pore-emanated cracking model would apply only if the stress-induced cracks can develop in a nonwelded tuff along weak interfaces (such as clast boundaries) under a significantly lower stress intensity factor (with a value of say, 0.1–0.2 MPa $m^{1/2}$).

[45] Another micromechanical model that has been used extensively for brittle faulting is the sliding wing crack model [*Horii and Nemat-Nasser*, 1986; *Ashby and Sammis*, 1990; *Kemeny and Cook*, 1991]. The model considers sources of tensile stress concentration that are located at the tips of preexisting cracks. The applied far-field stresses induce a shear traction on the crack plane (of length 2c), and if the resolved shear traction exceeds the frictional resistance along the closed crack, frictional slip occurs which also induces tensile stress concentrations at the two tips that may nucleate and propagate wing cracks to propagate parallel to the σ_1 direction. As wing cracks propagate to longer distances, they interact and ultimately coalesce to result in an instability. The model predicts that the maximum and minimum principal stresses at the onset of dilatancy and peak both fall on linear trends, and therefore if mechanical data on these critical stresses are available, then the model predictions can be tested and relevant micromechanical parameters inferred [*Ashby and Sammis*, 1990; *Baud et al.*, 2000a, 2000b; *Vajdova et al.*, 2004].

[46] However, there is a paucity of high-quality mechanical data for tuff that can be used this type of analysis. Very limited data on triaxial compression tests have been published, and they are not in a form that one can evaluate the critical stresses for the onset of dilatancy. As for our tuff samples, the brittle faulting regime falls on a very narrow pressure range and typically the amounts of dilatancy were almost negligible that it is difficult to pick out from our data the stress at the onset of dilatancy. To circumvent this difficulty, we will consider only the UCS here to assess whether the sliding wing crack model applies to our tuff data.

[47] At a fixed lateral stress, the sliding wind crack cracking model predicts that the peak differential stress scales with the parameter $K_{IC}/\sqrt{\pi c}$ [*Horii and Nemat-Nasser*, 1986; *Ashby and Sammis*, 1990; *Kemeny and Cook*, 1991]. The brittle strength is also predicted to decrease with increasing "initial damage" (or "crack density") which is characterized by a nondimensional parameter D_o, that is proportional to the number of preexisting cracks per unit area and the crack length squared (in the two-dimensional model). With reference to the sliding wing crack model of *Ashby and Sammis* [1990] and *Zhu* [2010] recently developed an analytic approximation for the UCS:

$$\sigma_u = \frac{1.346}{\sqrt{1+\mu^2}-\mu}\ \frac{K_{IC}}{\sqrt{\pi c}}\ D_0^{-0.256} \qquad (2)$$

where μ denotes the friction coefficient of the sliding crack.

[48] For a broad range of rock types (including granite, sandstone, limestone, gabbro, gneiss and basalt), values of μ inferred from dilatancy onset and peak stress data are in the range of 0.3–0.7, and of D_o in the range of 0.1–0.4. The preexisting microcracks we observed in Alban Hills tuff are relatively short with lengths on the order of 10 μm (Figure 4f). The longest have lengths of ~40 μm. Again assuming K_{IC} = 0.3 MPa $m^{1/2}$, the UCS can be estimated to be σ_u = 87 MPa from (2) using c = 20 μm, μ = 0.3 and D_o = 0.4. This estimate is significantly larger than the experimental measurements of 17.4 MPa and 33.4 MPa (Table 1). If we were to use a higher value of μ, a lower value of initial damage or a shorter crack length, the inferred UCS will be even higher. This discrepancy can be resolved only if K_{IC} has an unrealistically low value of ~0.1 MPa $m^{1/2}$, or if the preexisting sliding cracks have lengths up to 410 μm which are significantly longer than what we observed.

[49] The implication is that, between the two types of damage mechanics model, the pore-emanated cracking model is more viable than the sliding wing crack model as far as brittle failure in our nonwelded tuff is concerned. Although the sliding wing crack model by itself seems unlikely to control the brittle fracture development in Alban Hills tuff, we cannot rule out that it contributes to a certain extent as a mechanism coupled to pore-emanated cracking. While our analysis illustrates how certain constraints on the micromechanics of brittle failure in a porous tuff can be obtained from microstructural and mechanical data, it also underscores the limitation when one has data on samples from only one site, especially for a material with pore space as complicated as that of tuff.

[50] Preliminary microstructural observations reported in previous tuff studies [e.g., *Martin et al.*, 1994, 1995; *Moon*, 1993a] are not particularly useful for constraining the micromechanics of brittle failure. The Alban Hills tuff contains very few pumice vesicles, and yet microstructural observations on several naturally deformed nonwelded tuffs (Bishop tuff, CA; Bandelier tuff, NM; Busted Butte, NV) indicate that pumice collapse plays an important role in the failure process [*Evans and Bradbury*, 2004; *Wilson et al.*, 2003], which is not accounted for in the micromechanical model. We had access to the failed samples of Hong Kong tuff that were deformed by *Dobson and Nakagawa* [2005]. Thin sections of two samples (#2 and #4 with initial porosities of 1.86% and 4.58%, respectively) were prepared for microscope observations. We present in Figure 9 backscattered SEM images of these two samples. A throughgoing shear band had developed in HK tuff sample #2, which is located near the left edge of the image in Figure 9a. In its proximity, a complex network of pore-emanated cracks had propagated and coalesced, in qualitatively agreement with the pore-emanated cracking model. In contrast, HK tuff sample #4 failed by axial splitting and although we observed networks of microcracks in the vicinity of the axial fracture, most of the microcracks seem not to have initiated from stress concentrations near the larger pores (Figure 9b). It should also be noted that the larger pores in the HK tuff samples have dimensions on the order of 1–10 μm, significantly smaller than the range of 23 μm to 1.15 mm inferred from the UCS data on the basis of the pore-emanated cracking model. Unlike the samples we studied here, some tuffs may

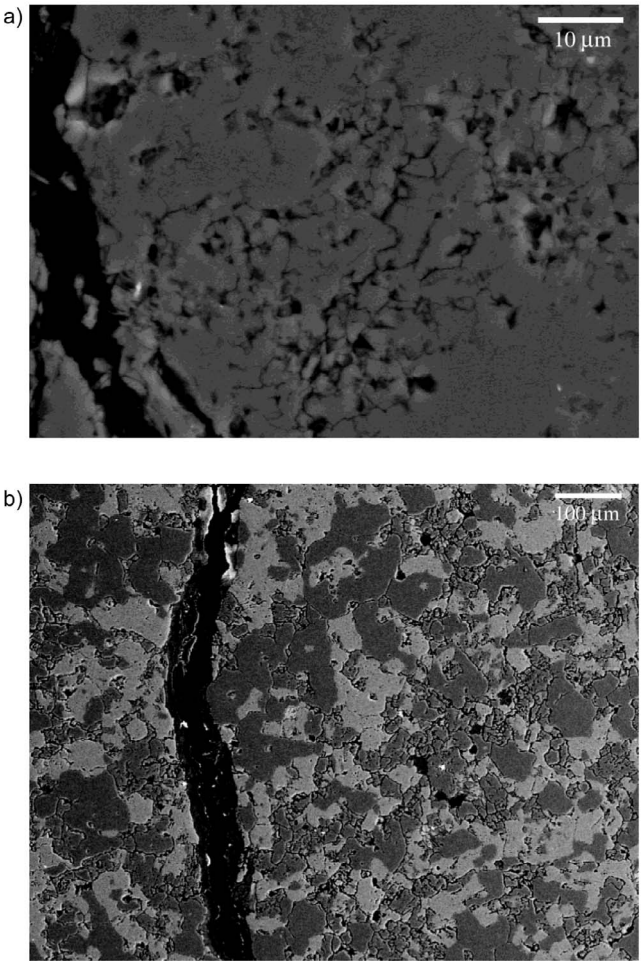

Figure 9. Backscatter SEM images of deformed samples of Hong Kong tuff. Direction of σ_1 is vertical. (a) HK #2 tuff (1.86% porosity) failed in uniaxial compression. The sample was loaded to the postpeak stage. A throughgoing shear band is visible on the left of the figure. Pores embedded in matrix have an average radius on the order of 1–10 μm. A complex of pore-emanated cracks had propagated and coalesced in the proximity of the shear band. (b) HK #4 tuff (4.58% porosity) failed in uniaxial compression. The failed sample is featured with axial splitting. The darker gray phase represents quartz, the lighter phase represents feldspar. Pores and splitting band appear black. Relatively equant pores are on the order of 10 μm. No obvious stress-induced cracks were observed to emanate from pores.

contain phyllosilicates and alteration minerals, and their presence can weaken the rock, resulting in significant scatter in the UCS as a function of porosity. Clearly more systematic studies of this nature are warranted to elucidate further the brittle failure mechanics of tuff.

5.2. Inelastic Compaction and Cataclastic Pore Collapse

[51] Our observations on inelastic compaction in Alban Hills tuff (Figure 7) indicate that it involves a pore collapse mechanism analogous to that in a porous limestone in two aspects. First, pore collapse tends to first initiate at the larger pores. Second, cataclasis and microcracking seem to be the dominant deformation mechanisms in the proximity of a pore that has collapsed. Relatively intense cracking would develop with a concentric halo surrounding the pore, and comminuted fragments may spall and fall into the void.

[52] *Zhu et al.* [2010] referred to this micromechanical process as "cataclastic pore collapse" and developed a model for its initiation. An externally applied stress field induces local stress concentration at the surface of a pore, and yielding initiates when the local stresses satisfy a specified failure criterion. Both the Mohr-Coulomb and Drucker-Prager yield criteria were considered. Similar to previous models of pore collapse [*Bhatt et al.*, 1975; *Gurson*, 1977; *Curran and Carroll*, 1979], the pores are idealized as spherical in shape.

5.2.1. Hydrostatic Compaction

[53] The mechanics of compaction is analyzed with reference to a representative element volume made up of a macropore embedded in an effective (porous) medium. If we first consider hydrostatic loading, the principal stresses $S_1 = S_2 = S_3 = P_c$ acts remotely on the external boundary of the element volume. It can be shown that local stresses in the vicinity of the pore are such that yielding will first occur at the spherical surface (Figure 10a). With reference to a cylindrical coordinate system (ρ, θ, z), the local stresses there are given by

$$\sigma_{\rho\rho} = 0 \tag{3a}$$

$$\sigma_{\theta\theta} = \sigma_{zz} = 3P_c/2 \tag{3b}$$

This stress state corresponds to an "unconfined compression," with a vanishing minimum principal stress. If one adopts the Mohr-Coulomb failure criterion (which is independent of the intermediate principal stress), the failure stress for the configuration (3) is identical to that for uniaxial compression. Accordingly, initial yielding (which signals the onset of cataclastic pore collapse) will occur when the maximum principal stress is equal to the UCS σ_u^* of the effective medium:

$$\sigma_{\theta\theta} = \sigma_{zz} = \sigma_u^* \;\Rightarrow\; P_c = P^* = 2\sigma_u^*/3 \tag{4}$$

A similar analysis can be performed for the Drucker-Prager criterion, which turns out to give an identical result for a remotely applied hydrostatic loading [*Bhatt et al.*, 1975; *Curran and Carroll*, 1979; *Zhu et al.*, 2010].

[54] In most previous analyses [*Bhatt et al.*, 1975; *Curran and Carroll*, 1979], it is implicitly assumed that the effective medium has a UCS (and other failure parameters) identical to those of the bulk sample, which would requires $\sigma_u^* = \sigma_u$. If indeed this assumption is valid, then (4) would imply that a plot of the pore collapse pressure P^* versus the UCS σ_u of the bulk sample falls on a linear trend with a slope of 2/3. To test this, we compile in Figure 10b tuff data of ours and other studies. *Lockner and Morrow* [2008] conducted a comprehensive series of measurements on nonwelded ignimbrites from Calico Hills, and *Aversa and Evangelista* [1998] presented data on the Neapolitan fine-grained tuff. The P^* and UCS values of Mt. Helen tuff were picked by us from Figure 8 of the report of *Heard et al.* [1973]. Porosities for the nonwelded ignimbrite samples compiled here range from

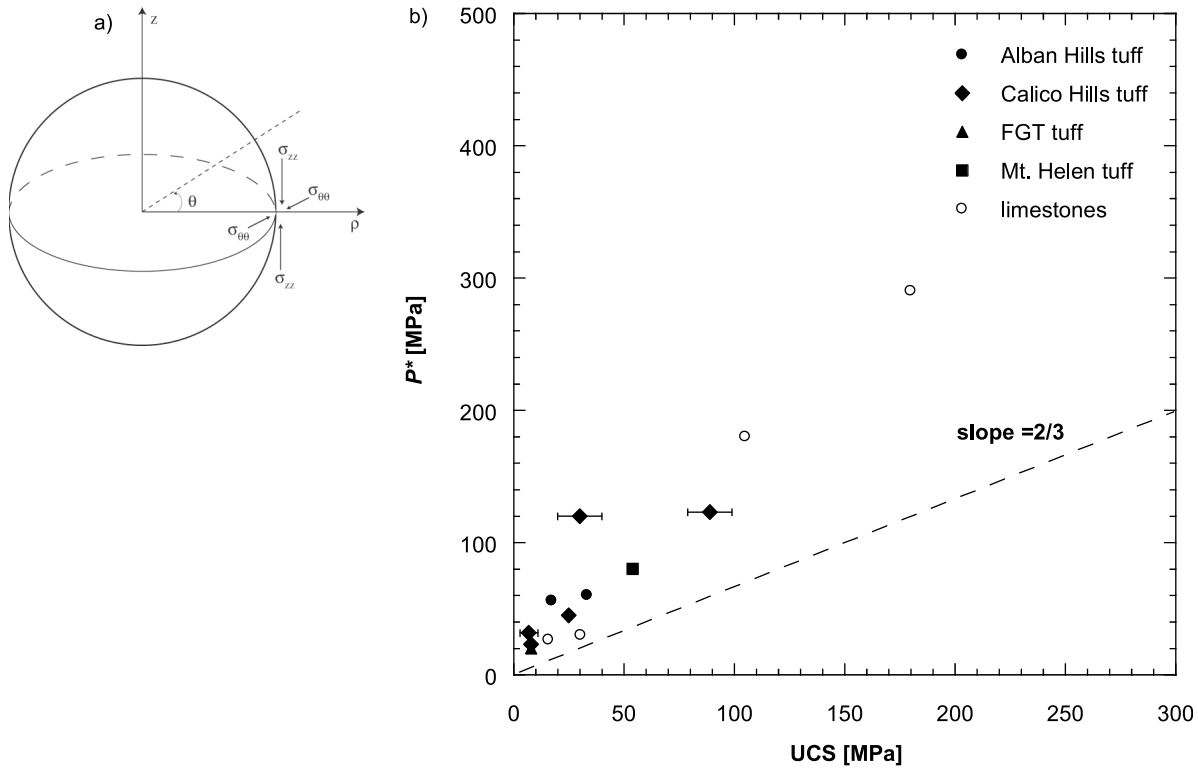

Figure 10. (a) Local stress field at the vicinity of the macropore. The local principal stresses σ_{zz} and $\sigma_{\theta\theta}$ act along the axial and azimuthal directions, respectively. Due to the boundary conditions in the pore surface, the radial stress is zero. (b) The critical pore collapse pressure P^* is plotted versus the uniaxial compressive strength UCS on nonwelded tuff samples. For comparison, limestone data compiled by *Zhu et al.* [2010] are also shown as open circles. The dashed line corresponds to a slope of P^* versus UCS equal to 2/3. The standard deviations of data on Calico Hills tuff are shown as error bars.

21.9% to 47.3%. For comparison, we also include limestone data that were compiled by *Zhu et al.* [2010].

[55] It can be seen that the tuff and limestone data all plot above the dashed line (with slope 2/3), which implies that $P^* = 2\sigma_u^*/3 > 2\sigma_u/3$, and therefore $\sigma_u^* > \sigma_u$ (Figure 10b). In other words, the effective medium is inferred to have a UCS that is much higher than that of the bulk sample. In light of our previous discussion of brittle failure in tuff, this implies that the effective medium is probably less porous than the bulk rock, a scenario that *Zhu et al.* [2010] postulated for limestone which is related to the dual porosity concept previously suggested in carbonate sedimentology [*Choquette and Pray*, 1970; *Pittman*, 1971; *Anselmetti et al.*, 1998; *Baechle et al.*, 2008].

[56] The total porosity Φ is assumed to be the sum of macroporosity Φ_M and microporosity Φ_m, made up of large and small pores with average diameters a and a^*, respectively. The partitioning of total porosity between Φ_M and Φ_m can be related to the microstructural data in Figure 5c. Our observations show that there are also numerous preexisting microcracks, but it is likely that the microcrack porosity contributes little to the total porosity. The effective medium is modeled as a porous medium that contains a population of micropores and microcracks (Figure 11a). Since the macropores have been excluded from it, the effective medium has a porosity less than the total porosity and accordingly its UCS σ_u^* is greater that the UCS σ_u of the bulk sample which includes the macropores.

[57] We will first analyze the effect of micropores on the UCS of the effective medium, following the approach of *Zhu et al.* [2010]. The average micropore size a^* is assumed to relatively small in comparison to average macropore size a and linear dimension b of the representative element volume, such that $b \gg a \gg a^*$. Brittle failure in the effective medium is assumed to be described by *Sammis and Ashby*'s [1986] pore-emanated cracking model, and therefore its UCS σ_u^* is given by equation (1) with $r = a^*$ and, on substituting into equation (4), we obtain the following relation between the pore collapse pressure P^* and total porosity:

$$P^* = \frac{2}{3}\sigma_u^* = \frac{0.883}{\Phi_*^{0.414}} \frac{K_{IC}}{\sqrt{\pi a^*}} = \frac{0.883}{\Phi^{0.414}} S^* \tag{5a}$$

with

$$S^* = \frac{K_{IC}}{\left(\Phi_*/\Phi\right)^{0.414}\sqrt{\pi a^*}} \tag{5b}$$

where Φ^* denotes the porosity of the effective medium, which is related to the macroporosity and microporosity by $\Phi^* = \Phi_m/(1 - \Phi_M) \approx \Phi_m$. Hence this micromechanical model for cataclastic pore collapse in a dual porosity medium pre-

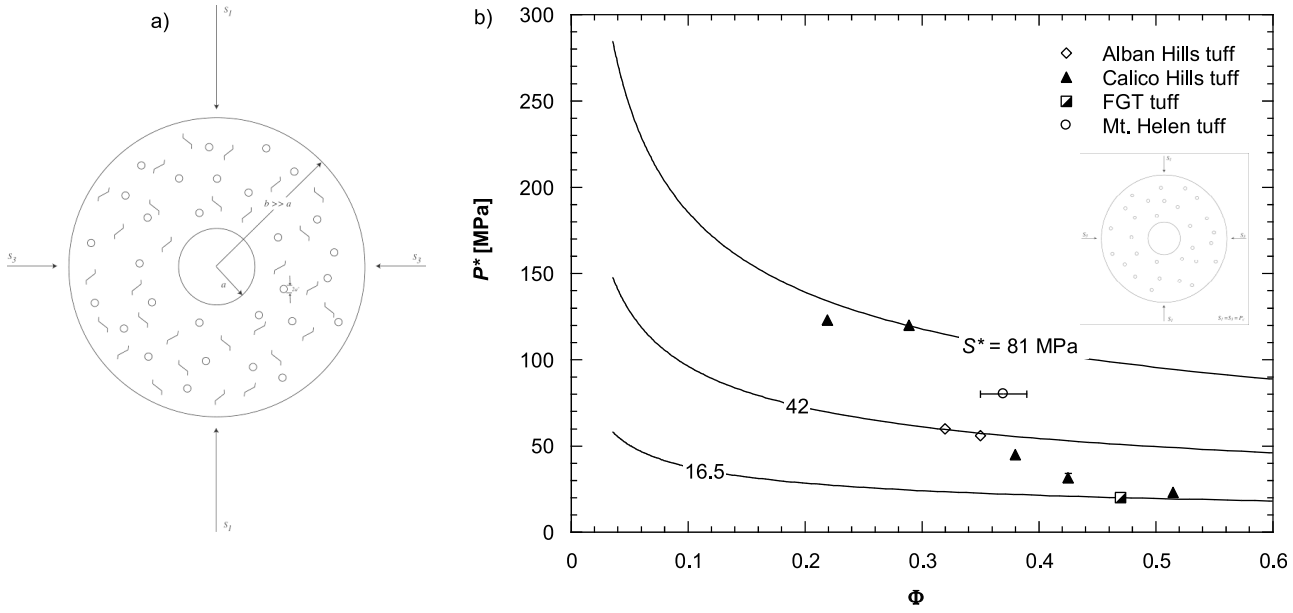

Figure 11. (a) Schematic diagram of a representative volume element of radius b. A macropore of radius a is surrounded by an effective medium made up of many micropores of radius a^* and preexisting microcracks with length of $2c$. Remote principal stresses are represented by S_1, S_2, and S_3. (b) Comparison of theoretical predictions with laboratory data on critical pore collapse pressure P^* of tuff samples when adopting dual porosity model with total porosity partitioned between macropores and micropores. Theoretical curves of P^* as a function of porosity for three different values of S^* are plotted. The data are bounded by upper and lower limits of S^* = 16.5 and 81 MPa. The standard deviations of data on Mt. Helen and Calico Hills tuff are represented by error bars.

dicts that while there is an overall decrease of the critical pressure with increasing porosity, the compactive yield stress is also dependent on the parameter S^* which characterizes the cooperative effect of micropore size, fracture toughness and partitioning of microporosity and macroporosity.

[58] In Figure 11b we plot our compiled P^* data versus total porosity. The data fall between two limiting curves accordingly to (5). The two Calico Hills tuff samples with lowest porosities (21.9% and 28.9%) lie on the upper curve corresponding to S^* = 81.0 MPa. Since $\pi a^* = (K_{IC}/S^*)^2 (\Phi/\Phi_*)^{0.828}$, the micropore diameter for this upper limit can be estimated to be $a^* \geq (K_{IC}/S^*)^2/\pi$ = 4.4 μm, assuming as before a K_{IC} value of 0.3 MPa m$^{1/2}$. The P^* data for the two samples with highest porosities (Neapolitan fine-grained tuff 47% and Calico Hills tuff 51.5%) seem to fall on a plateau given by the lower limit S^* = 16.5 MPa, which implies that $a^* \geq 105$ μm.

[59] Between the upper and lower limits, the inferred value of S^* decreases rapidly by a factor of ~5 with porosity increasing by a factor of 2.5 (Figure 11b). A similar trend in porous carbonate rock with the inferred S^* value decreasing with increasing porosity was reported by *Zhu et al.* [2010]. They also detected an approximately linear trend in the carbonate data, which is not obvious in our compiled tuff data.

[60] Our P^* values for dry Tufo del Palatino (Tdh1_PA) and Tufo Pisolitico (Tdh1_PI) samples fall on the theoretical curve for an intermediate value of S^* = 42 MPa, which implies that $a^* \geq 16$ μm (assuming K_{IC} = 0.3 MPa m$^{1/2}$ as before), comparable in dimension to many of the micropores we observed in the vicinity of a macropore (Figure 7). This comparison indicates that the pore-emanated cracking model provides a viable mechanism for cataclastic pore collapse in tuff when it is treated as a dual porosity medium made up of macropores and micropores.

[61] Microcracks were not considered to be important in the dual porosity model of *Zhu et al.* [2010], which was formulated with a porous limestone in mind. In the case of Alban Hills tuff, the density of preexisting cracks is high, even though many of them are relatively short. We next analyze the effect of these microcracks on the UCS of the effective medium, using as before the analytic approximation (2) obtained by *Zhu* [2010] for the sliding wing crack model. If the effective medium has a porosity that is dominated by microcracks with average length 2c, then its UCS σ_u^* is given by (2) and on substituting into (4), we obtain

$$P^* = \frac{2}{3}\sigma_u^* = \frac{0.897}{\sqrt{1+\mu^2}-\mu}\frac{K_{IC}}{\sqrt{\pi c}} D_0^{-0.256} \qquad (6)$$

[62] Since P^* values for our two dry tuff samples are 56 MPa and 60 MPa (Table 1), equation (4) implies that the UCS of the effective medium are 84 and 90 MPa. If we consider an effective medium made up of some of the longest preexisting microcracks (with $2c$~40 μm), then according to (2) its UCS can be estimated to be σ_u^* = 87 MPa (again assuming K_{IC} = 0.3 MPa m$^{1/2}$, μ = 0.3 and D_o = 0.4). That the two estimates of σ_u^* are almost identical suggest that, at least

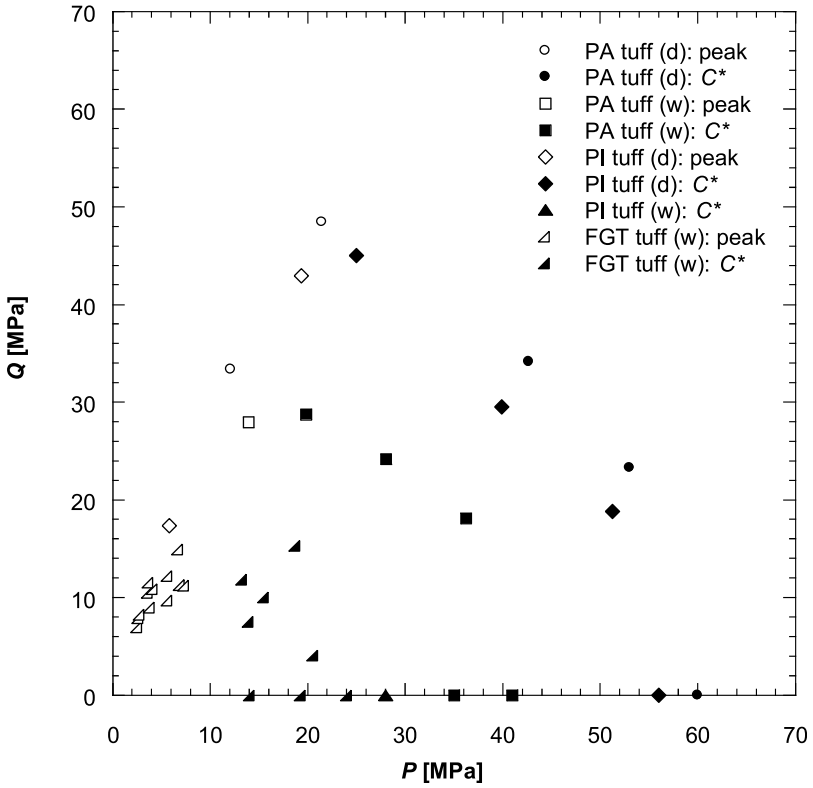

Figure 12. Peak stresses (open symbols) and critical stresses C^* (solid symbols) for the onset of shear-enhanced compaction are plotted in the P (mean stress) and Q (differential stress) space for Alban Hills tuff and Neapolitan fine-grained tuff [*Aversa and Evangelista*, 1998]. The peak stresses seem to follow Mohr-Coulomb criterion. There is an overall trend for the yield caps (C^*) to expand with decreasing porosity.

for Alban Hills tuff, sliding wing crack growth and coalescence can also provide a viable mechanism for cataclastic pore collapse in tuff, when it is treated as a dual porosity medium made up of macropores and microcracks. As noted earlier, this represents a limiting case in that if we were to use a higher value of μ or lower value of initial damage, the inferred UCS for the sliding wing crack model will be higher than that inferred from P^*.

[63] Our analysis of two types of mechanisms for cataclastic pore collapse has indicated that either the pore-emanated cracking or sliding wing crack model is consistent with our mechanical data and microstructural observations on Alban Hills tuff. We have assumed that the two mechanisms are decoupled, but in reality they probably operate as coupled processes that result in cataclastic damage leading to pore collapse.

5.2.2. Conventional Triaxial Compression

[64] We compile in Figure 12 the peak stresses and critical stress C^* for the onset of shear-enhanced compaction of Alban Hills tuff and Neapolitan fine-grained tuff [*Aversa and Evangelista*, 1998]. There is significant scatter in the latter set of data, possibly because the samples had variable initial porosity. Overall the C^* data are qualitatively similar in that they map out an elliptical cap in the effective mean stress (P) – differential stress (Q) space, that expands with decreasing porosity. The brittle strength data (in open symbols) show a positive correlation between P and Q, correspond to peak stresses that approximately follow the Mohr-Coulomb criterion.

[65] Under nonhydrostatic loading, the local stress field in the vicinity of a pore is more complicated. Furthermore, predictions of critical yielding stresses are fundamentally different according to whether Mohr-Coulomb or Drucker-Prager criterion is adopted. We consider a remote stress field $S_1 > S_2 = S_3$ applied to the representative volume element (Figure 10a), corresponding to a conventional triaxial compression test in the laboratory. With reference to a cylindrical coordinate system (ρ, θ, z), the local stress distribution is such that initial yielding will occur first along the equator of the sphere (at $z = 0$ and $\rho = a$), where the principal stresses are given by [*Timoshenko and Goodier*, 1951]

$$\sigma_1 = \sigma_{zz} = \frac{3}{2}\left[\frac{(9-5\nu)}{(7-5\nu)}(S_1 - S_3) + S_3\right] \tag{7a}$$

$$\sigma_2 = \sigma_{\theta\theta} = \frac{3}{2}\left[\frac{(5\nu-1)}{(7-5\nu)}(S_1 - S_3) + S_3\right] \tag{7b}$$

$$\sigma_3 = \sigma_{\rho\rho} = 0 \tag{7c}$$

[66] Substituting the (local maximum and minimum) principal stresses (7a) and (7c) into the Mohr-Coulomb

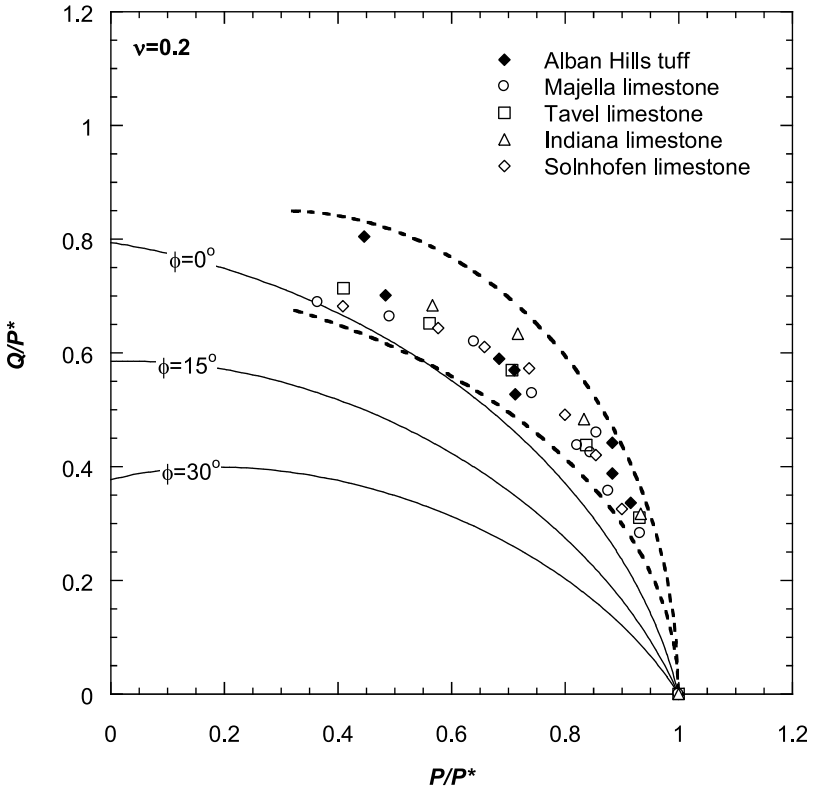

Figure 13. Differential stress (Q) and mean stress (P) at the onset of shear-enhanced compaction normalized by the pore collapse pressure P^*. The solid diamonds represent C^* of Alban Hills tuff normalized by a P^* of 41 MPa. For comparison, data on three limestone presented by *Zhu et al.* [2010] are also shown as open symbols. Normalized yield stresses of the four rocks fall on caps very close as bracketed by the dashed curves. Theoretical predictions according to the Drucker-Prager yield criterion (for a Poisson's ratio of 0.2) are plotted as solid curves. The angle of internal friction ϕ is marked on each curve.

criterion, *Zhu et al.* [2010] arrived at the following result for the critical stress state C^* at the onset of shear-enhanced compaction:

$$S_1 - S_3 = \frac{(7-5\nu)}{(9-5\nu)}\left(\frac{2}{3}\sigma_u^* - S_3\right) = \frac{(7-5\nu)}{(9-5\nu)}\left(P^* - S_3\right) \quad (8a)$$

where ν denotes Poisson's ratio of the effective medium. If we define $P = (S_1 + 2S_3)/3$ and $Q = S_1 - S_3$, then the stress state C^* can also be expressed as

$$Q = \frac{3(7-5\nu)}{10(2-\nu)}\left(P^* - P\right) \quad (8b)$$

This predicts that a plot of Q versus P falls on a straight line with a slope that falls on a narrow range of 0.9–1.05 for ν = 0–0.5. However, this amazingly simple prediction of a linear yield envelope is in discrepancy with laboratory observations. In recent years, a number of studies have been conducted to investigate the inelastic compaction behavior of porous siliciclastic and carbonate rocks [e.g., *Wong et al.*, 1997; *Vajdova et al.*, 2004; *Bemer et al.*, 2004; *Baud et al.*, 2006, 2009]. To our knowledge, most of the data for the onset of inelastic compaction fall on yield caps that are approximately elliptical in shape, except for an isolated study on Bleurswiller sandstone [*Fortin et al.*, 2006] which shows an apparently linear cap.

[67] Our analysis here implies that the intermediate principal stress (7b) cannot be neglected in analyzing the development of cataclastic pore collapse. We next consider the Drucker-Prager criterion which involves all three principal stresses in (6). For conventional triaxial compression, *Zhu et al.* [2010] derived this quadratic relation between the remotely applied mean stress P and differential stress Q at the onset of shear-enhanced compaction:

$$\begin{aligned}&(\alpha - \beta^2\gamma^2)Q^2 + \left[(3\beta - 4\beta\gamma^2)P - 2\beta\gamma(1-2\gamma)P^*\right]Q \\ &+ (1-2\gamma)\left(P - P^*\right)\left[(1+2\gamma)P + (1-2\gamma)P^*\right] = 0 \end{aligned} \quad (9)$$

with $\alpha = 100(7 - 13\nu + 7\nu^2)/[9(7 - 5\nu)^2]$, $\beta = 10(1 + \nu)/[9(7 - 5\nu)]$ and $\gamma = 2\sin\phi/(3 + \sin\phi)$, where ϕ denotes the angle of internal friction used in the Mohr-Coulomb criterion.

[68] In Figure 13 we replot our Alban Hills tuff data for C^* in Figure 12, with the differential stress and mean stress at the onset of shear-enhanced compaction normalized by the critical pressure for pore collapse from hydrostatic compression experiments. For comparison, we also include

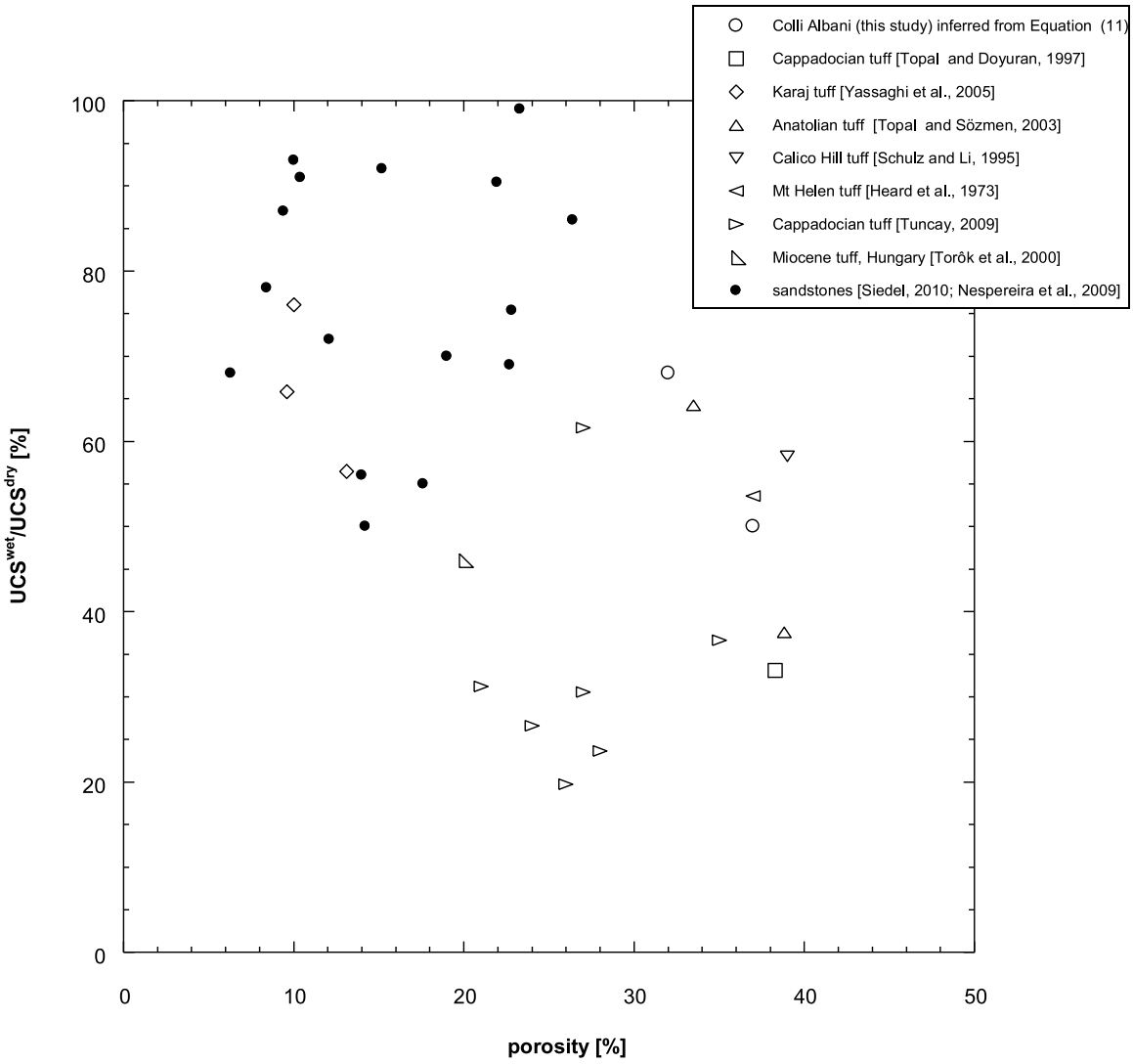

Figure 14. Ratio of UCS wet on UCS dry for various tuffs as a function of porosity (open symbols). For comparison, sandstone data from *Nespereira et al.* [2010] and *Siedel* [2010] are also shown as closed circles.

data for three porous limestones presented by *Zhu et al.* [2010]. Yield stress data for the normalized stresses Q/P^* and P/P^* of the four rocks fall on caps very close to one another. A similar behavior was observed for porous sandstones when the yield stresses were normalized by P^* [*Wong et al.*, 1997].

[69] For comparison, we show in Figure 13 the theoretical predictions of (9) according to the Drucker-Prager yield criterion (for a Poisson's ratio of 0.2) and three different angles of internal friction. *Zhu et al.* [2010] have shown that overall the effect of Poisson's ratio on the cap is relatively small. The nonlinear caps based on Drucker-Prager criterion are in qualitative agreement with laboratory data. The cap is predicted to expand with decreasing friction angle ϕ, and the highest differential stresses are associated with the cap for $\phi = 0$ (corresponding to the von Mises criterion), which shows the best quantitative agreement with experimental data, albeit at somewhat lower levels. For this limiting case, the differential stress Q as a function of the mean stress P is given by

$$\frac{Q}{P^*} = \frac{3}{20}\frac{(7-5\nu)}{(7-13\nu+7\nu^2)} \cdot \left[\sqrt{4(7-13\nu+7\nu^2) - 27\left(\frac{(1-\nu)P}{P^*}\right)^2} - (1+\nu)\left(\frac{P}{P^*}\right)\right] \tag{10}$$

with the pore collapse pressure P^* as a function of porosity given by either (5) or (6) for an effective medium dominated by micropores or microcracks, respectively.

[70] Our experimental data for tuff agree better with the theoretical prediction for very low values of ϕ. Just as in the limestone case that is an intriguing result. From what is known about the pressure sensitivity of brittle failure, one would expect the internal friction angle to be in the range of

10°–45° [*Zhu et al.*, 2010]. However, one should bear in mind that in the context of our dual porosity model, mechanical response in the effective medium made up of micropores or fine microcracks that should not be identical to that in the bulk sample involving larger macropores. Our analysis here would suggest that brittle failure in such an effective medium with numerous micropores and fine microcracks has a pressure sensitivity significantly lower than that of the bulk sample. To be consistent with the experimentally determined yield caps, our micromechanical model would require the effective medium to fail as a cohesive and pressure insensitive material.

5.3. Weakening of Tuff in the Presence of Water

[71] A weakening effect of water was observed at all tested pressure conditions in our block of PA tuff. Both the peak stress in the brittle regime and the onset of pore collapse C^* in the cataclastic flow regime occurred at lower differential stresses in the presence of water (Figure 2). The impact of water can be quantified in PA and PI tuffs by the ratio P^*_{wet}/P^*_{dry}, which provides a scaling of the difference between the dry and wet compactive envelopes. For PA tuff the critical pore collapse pressures for water saturated and dry conditions are 41 and 60 MPa, leading to P^*_{wet}/P^*_{dry} = 0.68, and we obtained P^*_{wet}/P^*_{dry} = 0.50 for the PI tuff (P^*_{wet} = 28 MPa and P^*_{dry} = 56 MPa). Water weakening was also reported by previous studies on sandstone [*Chester and Logan*, 1986; *Rutter and Mainprice*, 1978; *Baud et al.*, 2000a], granite [*Hadizadeh and Law*, 1991] and porous carbonates [*Baud et al.*, 2009]. In particular, *Baud et al.* [2000a] obtained values of the ratio P^*_{wet}/P^*_{dry} ranging from 0.70 to 0.96 in porous sandstone and more recently *Baud et al.* [2009] obtained 0.72 and 0.76 for two porous carbonates. The weakening effect of water appears therefore more pronounced in the tuff. While there is a paucity of dry/wet comparisons of triaxial and hydrostatic data on tuff, several studies compared the dry and wet UCS in this type of rock [*Heard et al.*, 1973; *Schultz and Li*, 1995; *Topal and Doyuran*, 1997; *Török et al.*, 2004; *Topal and Sözmen*, 2003; *Yassaghi et al.*, 2005; *Tuncay*, 2009]. In Figure 14, we compile previous data and show for reference representative data on sandstone [*Nespereira et al.*, 2010; *Siedel*, 2010]. In agreement with our triaxial data, the water weakening is, despite some scattering, overall significantly more important in tuff than in sandstone.

[72] *Baud et al.* [2000a] interpreted the effect of water observed in sandstone as mostly due to a reduction of the specific surface energy (and of the fracture toughness) and also to a reduction of the friction coefficient. If K'_{IC} and μ' are respectively the fracture toughness and the friction coefficient in the presence of water, the Hertzian fracture model developed by *Zhang et al.* [1990] predicts: $P^*_{wet}/P^*_{dry} = \left(\frac{K'_{IC}}{K_{IC}}\right)^3$. The inferred ratio K'_{IC}/K_{IC} was found for sandstone to be between 0.89 and 0.98. A consistent estimate was obtained from brittle data with a ratio μ'/μ of around 0.90 [*Baud et al.*, 2000a].

[73] The effective medium model with microporosity (5) and the pore crack model (1) both predict that the weakening effect of water observed in tuff is directly linked to K'_{IC}/K_{IC}. Moreover for a reasonable range of μ'/μ, one can assume that $\left(\sqrt{1+\mu'^2}+\mu'\right)/\left(\sqrt{1+\mu^2}+\mu\right) \sim 1$ and in first approximation the effective medium model with microcracks (6) and the wingcrack model (2) also predict that

$$\frac{P^*_{wet}}{P^*_{dry}} \sim \frac{\sigma_u^{wet}}{\sigma_u^{dry}} \sim \frac{K'_{IC}}{K_{IC}} \tag{11}$$

[74] We added in Figure 14 the ratio of UCS wet/dry for Alban Hills tuffs predicted by (11). Both points fall in the range found in previous studies. The micromechanical models suggest that the fracture toughness reduction due to water is significantly more important in tuff than in sandstone. It is likely however that other factors contribute to the observed weakening. First, as there are carbonatic inclusions in our samples, the weakening can also be related to the reaction between these particles and water. Second, we observed in the starting material (tuffIn) that tuff has many clasts and preexisting cracks embedded in the matrix. Under saturated conditions, water penetrates into the preexisting microcracks and reduces the friction between clasts embedded in the matrix. As the clasts are acting as obstacles to the crack propagation and coalescence according to our microstructural observations, the lubrication between clasts will therefore lead to a much easier propagation in saturated condition, which in turn results in a stronger water effect in tuff samples compared to sandstone and granite. The presence of some phyllosilicates and zeolitization may also enhance the water-weakening effect. Systematic measurements of dry and wet fracture toughness in tuff are however needed to further discuss the precise origin of water-weakening in these rocks.

6. Conclusion

[75] We investigated the deformation and failure modes of two tuffs from a borehole drilled in the Alban Hills volcanic complex (Rome, Italy). Our microstructural observations of intact samples with 32 and 37% average porosity show the geometric complexity of the pore space in these volcanic rocks, with macroporosity, microporosity and microcracks. Our new hydrostatic and triaxial compression data indicate that the phenomenology of deformation and failure in tuff is similar to that of sedimentary rocks. In the brittle regime, our microstructural observations emphasize the role of pores in the development of stress induced damage. As for inelastic compaction and cataclastic flow, our observations indicate that in some respects, the micromechanics in tuff is qualitatively similar to that documented recently in porous limestones, which typically involves pore collapse that initiates from stress concentrations at the periphery of the larger pores. Synthesizing published data, we observe a systematic trend for both uniaxial compressive strength and pore collapse pressure of nonwelded tuff to decrease with increasing porosity.

[76] To interpret the compaction behavior in tuff, we extended the cataclastic pore collapse model originally formulated for a porous carbonate rock to a dual porosity medium made up of macropores and micropores or microcracks. Our analysis has indicated that either the pore-emanated cracking or sliding wing crack model is consistent with our mechanical data and microstructural observations on Alban Hills tuff. Both models suggested that the signif-

icant weakening effect of water observed in these rocks could be the result of a large decrease of the fracture toughness in presence of water.

[77] **Acknowledgments.** We thank M. Mariucci, S. Pierdominici, P. Montone, and F. Marra for providing the cores from the S. Maria delle Mole scientific drilling project and for stimulating discussions on the material properties. We are grateful to Dave Lockner, who kindly provided the compaction data on Calico Hills tuff before publication. We thank Kam-Biu Luk, Pat Dobson, and Seiji Nakagawa for kindly providing their failed samples of Hong Kong tuff for microstructural observations. We are also grateful to Brian Bonner and Tom Dewers, who provided copies of the Lawrence Livermore and Sandia reports, respectively. We thank Jim Quinn for invaluable assistance with SEM microscopy. We have benefited from discussions with Joe Andrews, Cecilia Cheung, Dave Lockner, Seiji Nakagawa, and Robina Wong. This research was partially supported by the Office of Basic Energy Sciences, Department of Energy under grant DE-FG02-99ER14996.

References

Andrews, D. J. (2007), Compaction can limit peak vertical velocity at Yucca Mountain, *Eos Trans. AGU*, *88*(52), Fall Meet. Suppl., Abstract S14C-07.

Andrews, D. J., T. C. Hanks, and J. W. Whitney (2007), Physical limits on ground motion at Yucca Mountain, *Bull. Seismol. Soc. Am.*, *97*, 1771–1792, doi:10.1785/0120070014.

Anselmetti, F. S., S. Luthi, and G. P. Eberli (1998), Quantitative characterization of carbonate pore systems by digital image analysis, *AAPG Bull.*, *82*, 1815–1836.

Ashby, M. F., and C. G. Sammis (1990), The damage mechanics of brittle solids in compression, *Pure Appl. Geophys.*, *133*, 489–521, doi:10.1007/BF00878002.

Atkinson, B. K., and P. G. Meredith (1987), Experimental fracture mechanics data for rocks and minerals, in *Fracture Mechanics of Rock*, edited by B. K. Atkinson, pp. 477–525, Academic, London.

Avar, B. B., and N. W. Hudyma (2007), Observations on the influence of lithophysae on elastic (Young's) modulus and uniaxial compressive strength of Topopah Spring Tuff at Yucca Mountain, Nevada, USA, *Int. J. Rock Mech. Min. Sci.*, *44*, 266–270, doi:10.1016/j.ijrmms.2006.06.003.

Aversa, S., and A. Evangelista (1998), The mechanical behaviour of a pyroclastic rock: Yield strength and "destructuration" effects, *Rock Mech. Rock Eng.*, *31*, 25–42, doi:10.1007/s006030050007.

Baechle, G. T., A. Colpaert, G. P. Eberli, and R. J. Weger (2008), Effects of microporosity on sonic velocity in carbonate rocks, *Leading Edge*, *27*(8), 1012–1018, doi:10.1190/1.2967554.

Baud, P., W. Zhu, and T. Wong (2000a), Failure mode and weakening effect of water on sandstone, *J. Geophys. Res.*, *105*(B7), 16,371–16,389, doi:10.1029/2000JB900087.

Baud, P., A. Schubnel, and T. Wong (2000b), Dilatancy, compaction, and failure mode in Solnhofen limestone, *J. Geophys. Res.*, *105*(B8), 19,289–19,303, doi:10.1029/2000JB900133.

Baud, P., V. Vajdova, and T. Wong (2006), Shear-enhanced compaction and strain localization: Inelastic deformation and constitutive modeling of four porous sandstones, *J. Geophys. Res.*, *111*, B12401, doi:10.1029/2005JB004101.

Baud, P., S. Vinciguerra, C. David, A. Cavallo, E. Walker, and T. Reuschle (2009), Compaction and failure in high porosity carbonates: Mechanical data and microstructural observations, *Pure Appl. Geophys.*, *166*, 869–898, doi:10.1007/s00024-009-0493-2.

Bemer, E., O. Vincké, and P. Longuemare (2004), Geomechanical log deduced from porosity and mineralogical content, *Oil Gas Sci. Technol.*, *59*, 405–426.

Bhatt, J. J., M. M. Carroll, and J. F. Schatz (1975), A spherical model calculation for volumetric response of porous rocks, *J. Appl. Mech.*, *42*, 363–368, doi:10.1115/1.3423582.

Chester, F. M., and J. M. Logan (1986), Implications for mechanical properties of brittle faults from observations of the Punchbowl fault zone, California, *Pure Appl. Geophys.*, *124*, 79–106, doi:10.1007/BF00875720.

Choquette, P. W., and L. C. Pray (1970), Geologic nomenclature and classification of porosity in sedimentary carbonates, *AAPG Bull.*, *54*, 207–250.

Curran, J. H., and M. M. Carroll (1979), Shear stress enhancement of void compaction, *J. Geophys. Res.*, *84*(B3), 1105–1112, doi:10.1029/JB084iB03p01105.

de Rita, D., and C. Giampaolo (2006), A case study—Ancient Rome was built with volcanic stone from the Roman land, in *Tuffs—Their Properties, Uses, Hydrology, and Resources*, edited by G. Heiken, *Spec. Pap. Geol. Soc. Am.*, 408, 127–131.

Dobson, P., and S. Nakagawa (2005), Summary of rock-property measurements for Hong Kong tuff samples, *Rep. LBNL-58878*, 7 pp., Ernest Orlando Lawrence Berkeley Natl. Lab., Berkeley, Calif.

Evans, J. P., and K. K. Bradbury (2004), Faulting and fracturing of nonwelded Bishop tuff, eastern California: Deformation mechanisms in very porous materials in the vadose zone, *Vadose Zone J.*, *3*, 602–623, doi:10.2113/3.2.602.

Fisher, R. V., G. Heiken, and M. Mazzoni (2006), Where do tuffs fit into the framework of volcanoes?, in *Tuffs—Their Properties, Uses, Hydrology, and Resources*, edited by G. Heiken, *Spec. Pap. Geol. Soc. Am.*, *408*, 5–9.

Fortin, J., S. Stanchits, G. Dresen, and Y. Guéguen (2006), Acoustic emission and velocities associated with the formation of compaction bands in sandstone, *J. Geophys. Res.*, *111*, B10203, doi:10.1029/2005JB003854.

Funiciello, R., G. Heiken, R. Levich, J. Obenholzner, and V. Petrov (2006), Construction in regions with tuff deposits, in *Tuffs—Their Properties, Uses, Hydrology, and Resources*, edited by G. Heiken, *Spec. Pap. Geol. Soc. Am.*, *408*, 119–126.

Gurson, A. L. (1977), Continuum theory of ductile rupture by void nucleation and growth: Part I—Yield criteria and flow rules for porous ductile media, *J. Eng. Mater. Technol.*, *99*, 2–15, doi:10.1115/1.3443401.

Hadizadeh, J., and R. D. Law (1991), Water weakening of sandstone and quartzite deformed at various stress and stress rates, *Int. J. Rock Mech. Min. Sci.*, *28*, 431–439, doi:10.1016/0148-9062(91)90081-V.

Hamiel, Y., V. Lyakhovsky, and A. Agnon (2004), Coupled evolution of damage and porosity in poroelastic media: Theory and applications to deformation of porous rocks, *Geophys. J. Int.*, *156*, 701–713, doi:10.1111/j.1365-246X.2004.02172.x.

Heard, H. C., B. P. Bonner, A. G. Duba, R. N. Schock, and D. R. Stephens (1973), High pressure mechanical properties of Mt. Helen, Nevada, tuff, *Rep. UCID-16261*, 37 pp., Lawrence Livermore Lab., Univ. of Calif., Livermore, Calif.

Heiken, G. (Ed.) (2006), *Tuffs—Their Properties, Uses, Hydrology, and Resources*, *Spec. Pap. Geol. Soc. Am.*, *408*.

Hong Kong Geotechnical Control Office (1990), Foundation properties of marble and other rocks in the Yuen Long-Tuen Mun area, *Rep. 2/90*, 117 pp., Hong Kong Civ. Eng. Serv. Dep., Hong Kong.

Horii, H., and S. Nemat-Nasser (1986), Brittle failure in compression: Splitting, faulting and brittle-ductile transition, *Philos. Trans. R. Soc. London A*, *319*, 337–374, doi:10.1098/rsta.1986.0101.

Kemeny, J. M., and N. G. W. Cook (1991), Micromechanics of deformation in rocks, in *Toughening Mechanisms in Quasi-Brittle Materials*, edited by S. P. Shah, pp. 155–188, Kluwer Acad., Dordrecht, Netherlands.

Lockner, D. A., and C. A. Morrow (2008), Energy dissipation in Calico Hills tuff due to pore collapse, *Eos Trans. AGU*, *89*(53), *Fall Meet. Suppl.*, Abstract T51A-1856.

Long, J. C. S., and R. C. Ewing (2004), Yucca Mountain: Earth-science issues at a geologic repository for high-level nuclear waste, *Annu. Rev. Earth Planet. Sci.*, *32*, 363–401, doi:10.1146/annurev.earth.32.092203.122444.

Mariucci, M. T., S. Pierdominici, L. Pizzino, F. Marra, and P. Montone (2008), Looking into a volcanic area: An overview on the 350 m scientific drilling at Colli Albani (Rome, Italy), *J. Volcanol. Geotherm. Res.*, *176*, 225–240, doi:10.1016/j.jvolgeores.2008.04.007.

Martin, R. J., R. H. Price, P. J. Boyd, and J. S. Noel (1994), Bulk and mechanical properties of the Paintbrush tuff recovered from Borehole USW NRG-6, *Rep. SAND93-4020*, 99 pp., Sandia Natl. Lab., Albuquerque, N. M.

Martin, R. J., R. H. Price, P. J. Boyd, and J. S. Noel (1995), Bulk and mechanical properties of the Paintbrush tuff recovered from Borehole USW NRG-7/7A, *Rep. SAND94-1996*, 97 pp., Sandia Natl. Lab., Albuquerque, N. M.

Menéndez, B., W. Zhu, and T. Wong (1996), Micromechanics of brittle faulting and cataclastic flow in Berea sandstone, *J. Struct. Geol.*, *18*, 1–16, doi:10.1016/0191-8141(95)00076-P.

Mogi, K. (1964), Deformation and fracture of rocks under confining pressure (1), Compression tests on dry rock sample, *Bull. Earthquake Res. Inst. Univ. Tokyo*, *42*, 491–514.

Moon, V. (1993a), Microstructural controls on the geomechanical behaviour of ignimbrite, *Eng. Geol.*, *35*, 19–31, doi:10.1016/0013-7952(93)90067-M.

Moon, V. (1993b), Geotechnical characteristics of ignimbrite: A soft pyroclastic rock type, *Eng. Geol.*, *35*, 33–48, doi:10.1016/0013-7952(93)90068-N.

Nelson, P. H., and L. A. Anderson (1992), Physical properties of ash flow tuff from Yucca Mountain, Nevada, *J. Geophys. Res.*, *97*(B5), 6823–6841, doi:10.1029/92JB00350.

Nespereira, J., J. A. Blanco, M. Yenes, and D. Pereira (2010), Irregular silica cementation in sandstones and its implication on the usability as building stone, *Eng. Geol.*, *115*, 167–174, doi:10.1016/j.enggeo.2009.08.006.

Nimick, F. B., R. H. Price, R. G. van Buskirk, and J. R. Goodell (1985), Uniaxial and triaxial compression test series on Topopah Spring tuff from USW G-4, Yucca Mountain, Nevada, *Rep. SAND84-1101*, 111 pp., Sandia Natl. Lab., Albuquerque, N. M.

Palladino, D., M. Gaeta, and F. Marra (2001), A large K-foiditic hydromagmatic, eruption from the early activity of the Alban Hills volcanic district, Italy, *Bull. Volcanol.*, *63*, 345–359, doi:10.1007/s004450100150.

Paterson, M. S., and T. Wong (2005), *Experimental Rock Deformation—The Brittle Field*, 2nd ed., 348 pp., Springer, New York.

Pittman, E. D. (1971), Microporosity in carbonate rocks, *Am. Assoc. Pet. Geol. Bull.*, *55*, 1873–1878.

Price, R. H., and S. J. Bauer (1985), Analysis of the elastic and strength properties of Yucca Mountain tuff, Nevada, in *Proceedings of the 26th U.S. Symposium on Rock Mechanics*, edited by E. Ashworth, pp. 89–96, A. A. Balkema, Rotterdam, Netherlands.

Ricard, Y., and D. Bercovici (2003), Two-phase damage theory and crustal rock failure: The theoretical "void" limit, and the prediction of experimental data, *Geophys. J. Int.*, *155*, 1057–1064, doi:10.1111/j.1365-246X.2003.02112.x.

Riley, P. R., L. B. Goodwin, and C. J. Lewis (2010), Controls on fault damage zone width, structure, and symmetry in the Bandelier tuff, New Mexico, *J. Struct. Geol.*, *32*, 766–780, doi:10.1016/j.jsg.2010.05.005.

Russ, J. C. (1990), *Computer-Assisted Microscopy: The Measurement and Analysis of Images*, 453 pp., Plenum, New York.

Rutter, E. H., and D. H. Mainprice (1978), The effect of water on stress relaxation of faulted and unfaulted sandstone, *Pure Appl. Geophys.*, *116*, 634–654, doi:10.1007/BF00876530.

Sammis, C. G., and M. F. Ashby (1986), The failure of brittle porous solids under compressive stress states, *Acta Metall.*, *34*, 511–526, doi:10.1016/0001-6160(86)90087-8.

Schultz, R. A., and Q. Li (1995), Uniaxial strength testing of non-welded Calico Hills tuff, Yucca Mountain, Nevada, *Eng. Geol.*, *40*, 287–299, doi:10.1016/0013-7952(95)00041-0.

Siedel, H. (2010), Historic building stones and flooding: Changes of physical properties due to water saturation, *J. Perform. Constr. Facil.*, *24*, 452–461, doi:10.1061/(ASCE)CF.1943-5509.0000066.

Sleep, N. H. (2010), Sudden and gradual compaction of shallow brittle porous rocks, *J. Geophys. Res.*, *115*, B08210, doi:10.1029/2009JB006719.

Templeton, E. L., H. S. Bhat, R. Dmowska, and J. R. Rice (2010), Dynamic rupture through a branched fault configuration at Yucca Mountain, and resulting ground motions, *Bull. Seismol. Soc. Am.*, *100*, 1485–1497, doi:10.1785/0120090121.

Timoshenko, S., and J. N. Goodier (1951), *Theory of Elasticity*, 567 pp., McGraw-Hill, New York.

Topal, T., and V. Doyuran (1997), Engineering geological properties and durability assessment of the Cappadocian tuff, *Eng. Geol.*, *47*, 175–187, doi:10.1016/S0013-7952(97)00017-3.

Topal, T., and B. Sözmen (2003), Deterioration mechanisms of tuffs in Midas monument, *Eng. Geol.*, *68*, 201–223, doi:10.1016/S0013-7952(02)00228-4.

Török, A., M. Galos, and K. Kocsanyi-Kopecsko (2004), Experimental weathering of rhyolite tuff building stones and the effect of an organic polymer conserving agent, in *Stone Decay: Its Causes and Controls*, edited by B. J. Smith and A. V. Turkington, pp. 109–127, Donhead, Belfast, U. K.

Tuncay, E. (2009), Rock rupture phenomenon and pillar failure in tuffs in the Cappadocia region (Turkey), *Int. J. Rock Mech. Min. Sci.*, *46*, 1253–1266, doi:10.1016/j.ijrmms.2009.01.011.

Vajdova, V., P. Baud, and T. Wong (2004), Compaction, dilatancy, and failure in porous carbonate rocks, *J. Geophys. Res.*, *109*, B05204, doi:10.1029/2003JB002508.

Vajdova, V., W. Zhu, T.-M. N. Chen, and T. Wong (2010), Micromechanics of brittle faulting and cataclastic flow in Tavel limestone, *J. Struct. Geol.*, *32*, 1158–1169, doi:10.1016/j.jsg.2010.07.007.

Vinciguerra, S., P. Del Gaudio, M. T. Mariucci, F. Marra, P. G. Meredith, P. Montone, S. Pierdominici, and P. Scarlato (2009), Physical properties of tuffs from a scientific borehole at Alban Hills volcanic district (central Italy), *Tectonophysics*, *471*, 161–169, doi:10.1016/j.tecto.2008.08.010.

Wilson, J. E., L. B. Goodwin, and C. J. Lewis (2003), Deformation bands in nonwelded ignimbrites: Petrophysical controls on fault-zone deformation and evidence of preferential fluid flow, *Geology*, *31*, 837–840, doi:10.1130/G19667R.1.

Wong, T., C. David, and W. Zhu (1997), The transition from brittle faulting to cataclastic flow in porous sandstones: Mechanical deformation, *J. Geophys. Res.*, *102*(B2), 3009–3025, doi:10.1029/96JB03281.

Yassaghi, A., H. Salari-Rad, and H. Kanani-Moghadam (2005), Geomechanical evaluations of Karaj tuffs for rock tunneling in Tehran-Shomal freeway, Iran, *Eng. Geol.*, *77*, 83–98, doi:10.1016/j.enggeo.2004.08.003.

Zhang, J., T. Wong, and D. M. Davis (1990), Micromechanics of pressure-induced grain crushing in porous rocks, *J. Geophys. Res.*, *95*(B1), 341–352, doi:10.1029/JB095iB01p00341.

Zhu, W. (2010), Micromechanics of failure in porous carbonate and volcanic rocks, Ph.D. thesis, 201 pp., State Univ. of N. Y. at Stony Brook, Stony Brook.

Zhu, W., P. Baud, and T. Wong (2010), Micromechanics of cataclastic pore collapse in limestone, *J. Geophys. Res.*, *115*, B04405, doi:10.1029/2009JB006610.

P. Baud, Institut de Physique du Globe, UMR 7516 CNRS, EOST, Université de Strasbourg, Strasbourg F-67084, France. (patrick.baud@eost.u-strasbg.fr)

S. Vinciguerra, Istituto Nazionale di Geofisica e Vulcanologia, Sezione di Roma1, Via Nizza 128, I-00198 Rome, Italy.

T. Wong and W. Zhu, Department of Geosciences, State University of New York at Stony Brook, Stony Brook, NY 11794, USA.